Effect of the synthetic route on the structural, textural, morphological and catalytic properties of Iron(III) oxides and oxyhydroxides

Paula Oulego[a], *María A. Villa-García*[b]*, *Adriana Laca*[a] *and Mario Diaz*[a]

[a]Department of Chemical and Environmental Engineering, University of Oviedo.

[b]Department of Organic and Inorganic Chemistry, University of Oviedo.

c/ Julián Clavería s/n, 33071, Oviedo, Spain

*Corresponding author's e-mail: mavg@uniovi.es (M.A. Villa-García)

Phone: +34 985 10 29 76, FAX: +34 98510 34 46

Abstract

A variety of iron(III) oxides and oxyhydroxides were synthesised and characterised using three distinct methods of preparation: microemulsion, precipitation and sol-gel. The results clearly showed that the structure, textural properties, crystal morphology and catalytic performance of the phases obtained were highly dependent on the chemical routes used for the synthesis. Precipitation and microemulsion methods allowed obtaining mesoporous nanostructured iron(III) oxides with mean particle sizes of 4 nm (amorphous hematite) and 7 nm (ferrihydrite), which exhibited a high surface area (291.4 m^2/g and 192.3 m^2/g, respectively) and a very good catalytic behaviour in the advanced oxidation of non-biodegradable wastewaters. The different conditions employed in the synthesis of these materials through the sol-gel method yielded two goethites with practically the same catalytic properties, but dissimilar morphologies and texture. When soft agitation and slow addition of the precipitating agent were used, the resulting material (G1) was made up of shorter and finer particles, markedly acicular, with an average length of 400 ± 50 nm and width of 15 ± 5 nm. However, vigorous agitation and rapid addition of the precipitating agent led to the formation of longer and coarser particles, moderately acicular, the average length and width being 950 ± 100 nm and 140 ± 20 nm, respectively. The use of the sol-gel technique also resulted in the formation of a solid consisting of a mixture of hematite as main crystalline phase and goethite particles dispersed among the hematite particles. This solid presented a low specific surface area (13.2 m^2/g) and lower catalytic activity.

Therefore, precipitation and microemulsion proved to be the most suitable techniques to synthesise disordered iron(III) oxide nanoparticles catalytically active, due to the presence of highly reactive non-stoichiometric iron(III) ions, a higher surface area and smaller particle sizes.

1. Introduction

Iron(III) oxides are among the most widely used metal oxides with multiple applications in many scientific and industrial fields. Owing to their unique physical and chemical properties, iron oxides have been used as inorganic pigments, abrasive agents, high-density coatings, gas sensors, catalysts and precursors in the production of electronic, magnetic and non-linear optical devices.[1-4] It was also reported that super paramagnetic iron oxide nanoparticles, after appropriate surface functionalization, can be used for numerous biomedical applications.[5-6]

Due to their catalytic properties, iron(III) oxides are used in many important reactions of the chemical industry, such as in the Fischer-Tropsch synthesis of hydrocarbons,[7,8] photocatalytic water splitting,[9] synthesis of ammonia,[10] vapor-phase oxidation of benzoic acid to phenol[11] and styrene production.[12] Based on the estimations of the World Health Organization, half of the world's population will be living in countries or regions experiencing water scarcity by 2025. Therefore, it is necessary to develop strategies for the treatment of wastewaters in order for the treated ones to be reused as much as possible. For this reason, in the last few decades, iron compounds have also been tested as catalysts for the removal of hazardous contaminants from wastewaters in advanced oxidation processes[13,14] and, namely, in catalytic wet air oxidation processes.[15,16]

Catalytic wet oxidation (CWO) is a promising technology for the treatment of non-biodegradable organic pollutants in wastewaters. Application of adequate catalysts to wet oxidation technologies reduces energy requirements and favours the achievement of considerably higher oxidation rates, even for pollutants which are oxidised with difficulty. In the CWO process organic contaminants are partially oxidised to innocuous compounds such as CO_2, H_2O and dissolved hetero ions at much lower temperatures and pressures than in non-catalysed processes and, consequently, operational costs are

considerably reduced.[15-17] However, complete oxidation of many organic pollutants is hard to achieve due to the formation of intermediates which exhibited a great resistance to oxidation. Therefore, it is necessary to develop long life active catalysts that can be effectively utilised for wastewater treatment on industrial scale.

Iron oxides are desirable catalysts in terms of cost and resistance to poisoning, though their activities are still lower than that of noble metals. The catalytic activity depends on the chemical nature and the structural and textural properties of the heterogeneous catalyst. Thus, the catalytic performance and the stability can be improved significantly by using preparation methods which allow for good control of the geometry and texture of the active phases. Iron oxides can be prepared by different synthetic procedures, such as sol-gel reactions,[18] precipitation,[19] microwave synthesis,[20] hydrothermal and solvothermal synthesis,[13,21,22] and microemulsion.[23,24] Microemulsion technique was proven to be very successful in preparing high surface area metal oxides.[24] The sol-gel process is an extremely versatile technique that allows the formation of a large variety of metal oxides at relatively low temperatures. Precipitation is frequently used for the synthesis of a wide variety of compounds; however, control of particle size is limited when using this technique because only kinetic factors are controlling the growth of the crystal.

As far as we know, there are no previous studies focused on the analysis of how the structure, texture, morphology and catalytic activity of various iron-bearing phases can be affected by the selection of a specific synthetic route. Moreover, there are no studies dealing with the use of iron(III) oxides or oxyhydroxides as heterogeneous catalysts for the degradation of landfill leachates by wet oxidation. In this regard, the use of iron oxides as heterogeneous catalysts has mainly been reported for the photodegradation of dyes and the oxidation of alcohols and olefins.[13,25-27] Therefore, the aim of this work was to

evaluate the influence of the synthesis conditions on the structure, textural properties, morphology and catalytic performance as heterogeneous catalysts in CWO processes, of various iron oxides and oxyhydroxides obtained using different synthesis procedures: microemulsion, sol-gel and precipitation techniques. Variables such as the chemical nature of the precursors, reactants concentration, flow rate and stirring speed of the reaction were considered. The samples were characterised by X-ray diffraction, Mössbauer and FTIR spectroscopy, N_2 adsorption-desorption at 77 K, EDX, SEM and TEM microscopy and SAED. Catalytic activity was studied by means of wet oxidation tests of highly-contaminated landfill leachates, which were carried out at 180ºC, 6.0 MPa and pH=6.9.

2. Experimental

2.1. Reagents

All reagents were purchased from Sigma-Aldrich, namely $Fe(NO_3)_3 \cdot 9H_2O$ and $FeCl_3 \cdot 6H_2O$ (puriss. grade), the non-ionic surfactant Brij 58, isopropyl alcohol (ACS reagent >99.5%), ammonia solution (25% wt.) and NaOH pellets (reagent grade).

2.2. Synthesis of iron(III)oxides/oxyhydroxides

Preparation of iron(III)oxide nanoparticles by a microemulsion route.

A microemulsion was prepared by mixing the non-ionic surfactant Brij 58, isopropyl alcohol and an aqueous solution of $Fe(NO_3)_3 \cdot 9H_2O$. The surfactant concentration was 0.15 mol/L, the hydrated ferric nitrate concentration was 0.24 mol/L, and the water-to-surfactant molar ratio was 18.5. To this microemulsion was added, drop by drop (2 mL/min) and under vigorous stirring (1000 rpm), 11.4 M ammonia solution until the pH was 8.0. The reaction mixture was kept under stirring for 5 h, and then aged at 55ºC in a closed Pyrex bottle for 3 days. The precipitate obtained was centrifuged; thoroughly

washed with distilled water and dried at 55ºC for 12 h. The solid was suspended in 75 mL of acetone and stirred at room temperature for 18 h, then it was centrifuged, washed with distilled water, dried at 55ºC for 12 h and heated 4 hours at 300ºC.

Preparation of iron oxides by precipitation.

Sample H1 was prepared by adding an ammonia solution (15 % wt) drop wise (6.5 mL/min) under continuous stirring (750 rpm) to a $FeCl_3 \cdot 6H_2O$ solution (0.5 M) until the pH of the medium was 9.0. Sample H2 was obtained by mixing under continuous stirring (750 rpm) 1 M $Fe(NO_3)_3 \cdot 9H_2O$ solution with 5 M NaOH solution. The reaction mixtures of both samples H1 and H2 were aged at room temperature for 3 h, then the precipitates were washed with distilled water, centrifuged and dried at 120ºC for 12 h. Besides, the precipitated from H2 was air heated at 300ºC for 4 h.

Preparation of iron(III) oxyhydroxides by sol-gel method.

Three iron oxides/oxyhydroxides, samples GH, G1 and G2, were prepared using a modification of the Sugimoto method.[28] Sample GH was obtained as follows: to 50 mL of 2 M $FeCl_3 \cdot 6H_2O$ solution were added drop by drop (2.5 mL/min) 50 ml of 5 M NaOH solution at room temperature and under continuous stirring (400 rpm). Samples G1 and G2 were obtained by adding to 50 mL of 2 M $FeCl_3 \cdot 6H_2O$ solution 50 mL of 6 M NaOH solution, at room temperature. The base was added drop by drop under different conditions: slowly (1.5 mL/min) and under gentle stirring (250 rpm) for sample G1; quickly (3.5 mL/min) under vigorous stirring (750 rpm) for sample G2. Once the highly viscous gels were obtained (consisting of $Fe(OH)_3$ and Fe^{3+}), the stirring used in each case was continued for 30 min. Then, the gels were aged at 95ºC for 7 days, cooled and kept at room temperature for 24 h, centrifuged, washed with distilled water and dried for 12 hours at 120ºC.

2.3. Techniques of characterization

Powder X-ray diffraction (XRD) patterns were obtained with a PANalyticalX´Pert Pro powder diffractometer using Cu Kα radiation ($\lambda_{K\alpha}$ = 1.5406 Å) and a graphite secondary monochromator. Diffractograms were recorded for 2θ values between 10º and 80º by 0.02º step, with a scan step time of 1 s. The iron content of the samples was determined by ICP mass spectrometry (ICP-MS), using an Agilent 7500ce spectrometer. Rhodium (^{103}Rh) was used as internal standard. The instrumental parameters for ICP-MS are shown in the Supplementary Information (Table S1). All samples were digested by acid assisted microwave irradiation using Perkin Elmer Multiwave 3000. 8 mL of aqua regia (3HCl:1HNO_3 mixture) were added to 100 mg of each of the samples (previously ground to < 75 μm) in closed Teflon vessels. The microwave program consisted of subjecting the sample to a power of 600 W for 8 min. A Perkin Elmer 2400 analyzer with a Perkin Elmer AD-2Z microbalance was used to determine the hydrogen content of the solids. Mössbauer spectroscopy was performed at room temperature in the transmission geometry using a conventional constant-acceleration spectrometer with a ^{57}Co-Rh source. The isomer shift was taken with respect to a bcc-Fe calibration foil measured at room temperature. FTIR spectra of the samples were recorded in the 4000 - 400 cm^{-1} range, by means of a Perkin-Elmer PARAGON 1000 spectrometer. The resolution employed was 4 cm^{-1}. The specimens were pressed into small discs using a spectroscopically pure KBr matrix. Specific surface area and porous structure was studied by nitrogen adsorption at 77 K. Nitrogen adsorption–desorption isotherms at 77 K were obtained with a Micromeritics ASAP 2020 instrument, using static adsorption procedures. Before the analysis, the samples were degassed at 120 °C for 10 h. Analysis of mesoporosity was performed through the BJH method.[29] The microscopic morphology of the samples and energy dispersive X-ray (EDX) analyses were performed using a JEOL JMS-6610LV

scanning electron microscope (SEM) operating at 0.3–30 kV. Previously to the SEM characterization and EDX analysis, the iron oxides were sputtered coated with gold to make them electrically conductive. Transmission electron microscopy (TEM) was performed on a MET JEOL-2000 EX-II microscope and selected area electron diffraction (SAED) was acquired on a MET JEOL-JEM 2100F with an operating voltage of 200 kV. Samples were prepared by sonicating the powdered sample in ethanol and then evaporating two droplets on carbonated copper grids.

2.4. Catalytic experiments: apparatus and procedure

The catalytic tests were performed in a 1 L semi-batch reactor (Parr T316SS) equipped with two six-bladed magnetically driven turbine agitators. The procedure is described with more detail in Oulego et al. (2015).[30] In a typical experiment, 0.7 L of stabilised landfill leachate and the iron catalyst (350 mg) were introduced into the reaction vessel, which was then heated and pressurised to the operating conditions under a continuous oxygen flow (2.33×10^{-5} Nm^3/s). The oxygen was bubbled through the water reservoir in order for it to become saturated with water vapour before being sparged into the reaction vessel. A valve and a coil fitted to the top of the vessel allowed the collection of samples during the reaction. Reaction temperature and pressure were maintained constant during the course of each experiment. Two bubblers filled with a concentrated solution of sulphuric acid and another two bubblers filled with a concentrated solution of sodium hydroxide were installed at the end of the gas line with the purpose of absorbing ammonia or carbonates, in case these species were formed.

2.5. Analytical methods

Chemical oxygen demand (COD) concentration was determined by the dichromate method (at 600 nm) according to Standard Methods[31] using a DR2500 spectrophotometer (Hach Company, USA). A Shimadzu TOC-V_{CSH} analyzer (Shimadzu, Japan) was used to

182 determine total organic carbon (TOC). Biochemical oxygen demand (BOD_5) was
183 measured using a manometric respirometric measurement system, BOD-System
184 OxiDirect® (Lovibond, Germany). pH was determined by means of a pH-meter Jenway
185 3510. Vibrio fischeri was used to assess the bacterial toxicity of the treated landfill
186 leachate according to ISO 11348-3.[32] A description of the procedure used appears in the
187 Supplementary Information (section 2). Changes in the colour of the leachate during its
188 oxidation were also monitored by tracking the evolution of the colour number (CN). The
189 calculation of this parameter is described in section 3 of the Supplementary Information.
190 All analytical measurements were done at least in triplicate.

191 **3. Results and discussion**

192 *3.1. Structural characterization. X-ray diffraction*

193 XRD was performed to obtain the crystalline structure of the solids. The diffraction
194 patterns of the iron oxides and hydroxides obtained using different synthesis procedures
195 are shown in Figure 1.

196 The XRD pattern of sample Fh, Figure 1A, shows two low intensity broad peaks
197 indicating a low crystal order. The d-values corresponding to the diffraction peaks are
198 2.51 Å (110) and 1.45 Å (300), which correspond to the d-spacing of poorly ordered two-
199 line ferrihydrite.[33,34] Tüysüz et al.[34] reported that the low crystal order of ferrihydrite is
200 the consequence of both a poorly defined stoichiometry and a not very well established
201 atomic structure. Although different chemical formulas have been proposed for
202 ferrihydrite, such as $Fe_5HO_8 \cdot 4H_2O$, $5Fe_2O_3 \cdot 9H_2O$[35] and $Fe_{10}O_{14}(OH)_2$,[36] no single
203 formula is widely accepted for ferrihydrite.

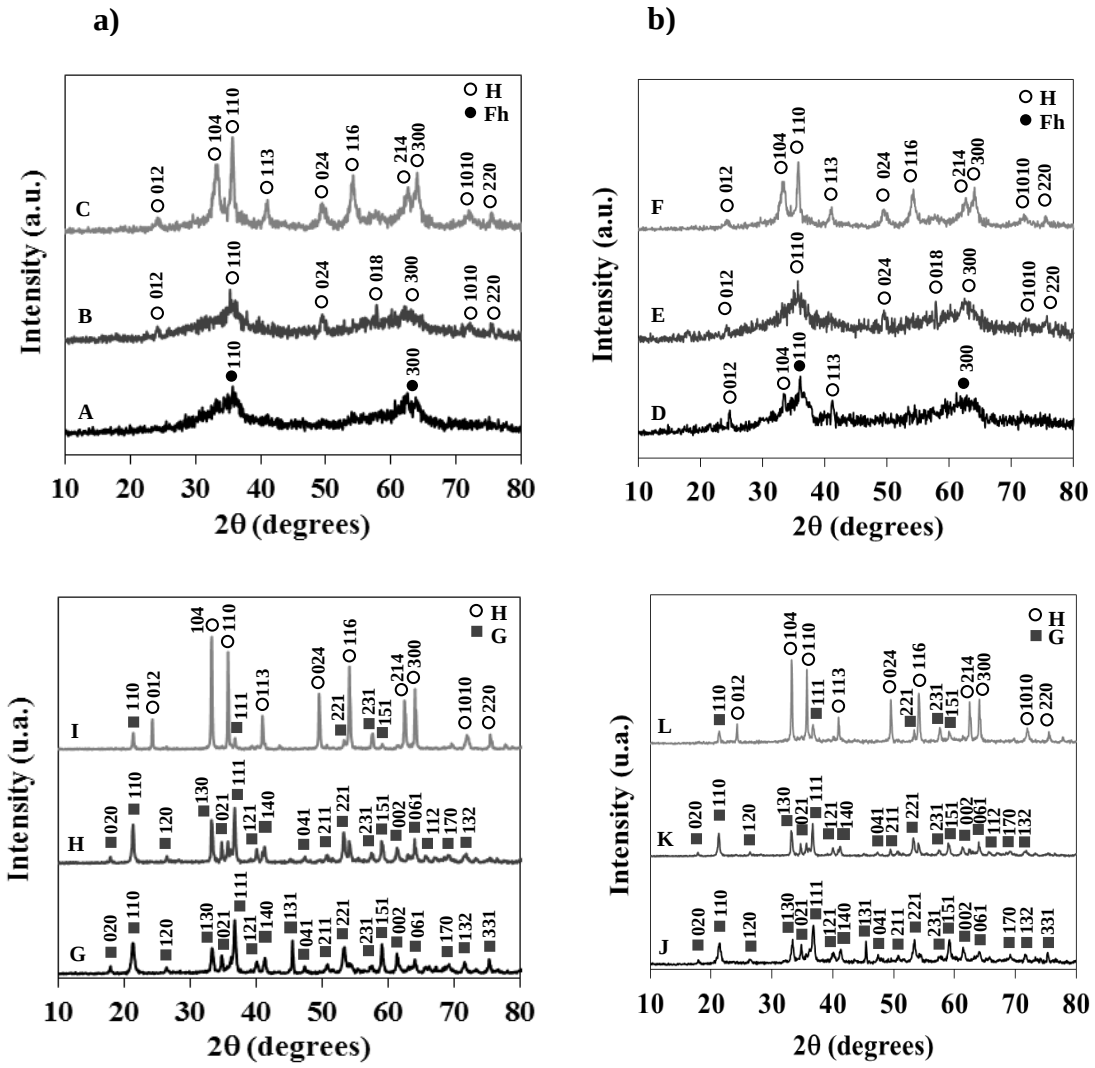

Figure 1. a) XRD patterns of the solids before catalytic wet oxidation: Fh (A), H1 (B), H2 (C), G1 (G), G2 (H) and GH (I), and b) XRD patterns of the solids after catalytic wet oxidation: Fh (D), H1 (E), H2 (F), G1 (J), G2 (K) and GH (L). In all cases, H, Fh and G indicate phases of hematite, ferrihydrite and goethite, respectively.

This is attributed to variable water content as well as to the difficulty of obtaining accurate structural characterization. Michel et al.[36] reported in a detailed structural analysis of ferrihydrite that Fe^{3+} ions are octahedrally coordinated within the hexagonal unit cell, but are tetrahedrally coordinated at the ferrihydrite surface. The large surface area of this nanocrystalline material and the increased reactivity of the coordinatively unsaturated surface Fe^{3+} ions can confer very interesting catalytic properties to

ferrihydrite. Additional characterization of this sample was obtained from its Mössbauer spectrum recorded at room temperature.

Figure 1B and 1C show the diffraction lines of two iron oxides, samples H1 and H2, obtained by precipitation of Fe(III) salts with ammonia and NaOH solutions, respectively. The XRD pattern of sample H1, Figure 1B, is characteristic of a very poorly ordered material; the diffractogram showed a low intensity broadened diffraction peaks at around 36° and 63º (2θ) ascribed to amorphous hematite particles.[37] Another peaks of low intensity can also be distinguished at 24.1º, 49.5º. 57.8º, 72.1º and 75.4º. Various authors have reported the presence of such peaks in hematite particles, although the intensity of peaks was greater than those found in this study, which is due to the higher crystallinity of such particles[18,38,39].

Since H1 exhibited very poor crystallinity, the electron diffraction pattern was performed (see Figure S1). Such diffraction pattern was analysed with Diffraction Ring Profiler, which was developed for phase identification in complex microstructures[40]. All of the observed Debye rings can be matched to that of a rhomboedral hematite, JCPDS no. 33-0664, with cell constants a = 5.0356 Å and c = 13.7489 Å. This result is in agreement with the peak positions displayed in the XRD spectrum. Additional structural information of this phase was obtained from Mössbauer spectroscopy, since Mössbauer parameters allow distinguishing amorphous Fe_2O_3 from other iron(III) oxide polymorphs (α-Fe_2O_3, β-Fe_2O_3, γ-Fe_2O_3 and ε-Fe_2O_3). The XRD pattern of sample H2, Figure 1C, showed the diffraction peaks at 24.1º, 33.4º, 35.7º, 41.1º, 49.5º, 54.2º, 62.6º, 64.1º, 72.1º and 75.4º, which are characteristic of a pure α-Fe_2O_3 phase (JCPDS no. 33-0664); however, the broadened diffraction lines indicates the formation of poorly ordered hematite and/or the presence of very fine hematite particles.[18,38,39,41]

238 The XRD patterns of samples G1 and G2 are depicted in Figure 1G and 1H,
239 respectively. All of the strong sharp diffraction peaks can be indexed as the pure
240 orthorhombic phase of goethite with cell constants a = 4.608 Å, b = 9.956 Å and c = 3.021
241 Å (JCPDS no. 29-0713), showing the most intense peak at 36.7º. These data are in
242 accordance with those found in the literature.[19,42,43] The results revealed the high purity
243 of G1 and G2, since no diffraction peaks of impurity phases were detected. The diffraction
244 lines of sample GH, Figure 1I, are characteristic of a highly ordered solid. The peaks that
245 appear at 24.1º, 33.4º, 35.7º, 41.1º, 49.5º, 54.2º, 62.6º, 64.1º, 72.1º and 75.4º are
246 characteristic of rhombohedral hematite[18,38,39,41]. Lower intensity peaks at 21.3º, 36.7º,
247 53.3º, 57.6º and 59.2º are indicative of the presence of orthorhombic goethite as a
248 minority phase[19,42,43].
249 The XRD patterns of all the samples after using them as catalysts are shown in Figure
250 1b. The diffractogram of the used ferrihydrite, Figure 1D, shows new sharp peaks at 24.1º,
251 33.4º and 41.1º, which indicate the incipient formation of highly ordered hematite.
252 Therefore, ferrihydrite was partly transformed into hematite after catalytic reaction.
253 Schwertmann et al.[44] reported that the convertibility to hematite is very high for two-line
254 ferrihydrite in an aqueous system, even at low temperature. The XRD patterns of the other
255 used catalysts did not show any phase changes (Figure 1b). However, the diffraction lines
256 were slightly sharper, indicating a little increase in the crystal order of the iron(III)
257 oxides/oxyhydroxides under the catalytic process conditions.

258 *3.2. Chemical composition of iron(III) oxides and oxyhydroxides*

259 The iron and hydrogen content of the iron(III) oxides and oxyhydroxides is shown in
260 Table 1.

Table 1. Iron, hydrogen and oxygen content of the iron(III) oxides and oxyhydroxides.

Sample	Iron content[a] (%)	Hydrogen content[b] (%)	Oxygen content[c] (%)
Fh	**68.93 ± 0.03**	**0.24 ± 0.01**	**30.83 ± 0.04**
H1	**68.95 ± 0.06**	**0.00**	**31.05 ± 0.06**
H2	**68.20 ± 0.10**	**0.00**	**31.80 ± 0.10**
G1	**63.45 ± 0.09**	**0.93 ± 0.01**	**35.62 ± 0.10**
G2	**63.03 ± 0.07**	**0.96 ±0.01**	**36.01± 0.08**
GH	**67.79 ± 0.06**	**0.22 ± 0.01**	**31.99± 0.07**

[a]From ICP-MS analysis. [b]From elemental analysis. [c]calculated by difference.

Taking into account these data, the empirical formulas of the iron-bearing phases were determined. Thus, the formulas for the iron oxides H1 and H2 were $Fe_2O_{3.14}$ and $Fe_2O_{3.25}$, respectively, which agrees well with the expected stoichiometry (Fe_2O_3). Tadic et al.[45] proposed $Fe_{1.88}O_3$ as the empirical formula of hematite nanoparticles obtained by hydrothermal method. For ferrihydrite, the calculated formula was $Fe_{10.4}O_{14.2}(OH)_2$, which is nearly the same as one of the formulas proposed by Michel et al.: $Fe_{10}O_{14}(OH)_2$.[36] With regard to oxyhydroxides, G1 and G2, the formulas obtained were $Fe_{1.23}O_{1.42}(OH)$ and $Fe_{1.19}O_{1.37}(OH)$, respectively. Regarding GH oxide, in order to obtain the empirical formula, the intensity ratio of the most intense XRD peaks of hematite and goethite was used, this ratio being 6.72 (Figure 1). Based on this value, the calculated formula was $FeOOH \cdot 6.72\ (Fe_2O_3)$, the iron percentage being 69.40%, which is in good agreement with the iron content measured by ICP-MS (67.79%).

EDX analysis of the iron(III) oxides and oxyhydroxides were also performed as shown in Figure S2 of the Supplementary Information. In all cases, the analysis revealed only the presence of Fe and O in the formed microstructures. This means that neither nitrate nor chloride contamination was detected. The atomic ratios Fe/O for samples H1, H2, Fh, G1 and G2 were 39:61, 38:62, 39:61, 34:66 and 33:67, respectively, which are in agreement with those obtained from the formulas determined previously. The value of

the ratio for H1 and H2 is also in accordance with that reported by Tadic et al.[45] in the abovementioned study. Two different EDX analyses were carried out on the GH sample, due to the fact that it is composed of a mixture of hematite and goethite. The first analysis was performed on the acicular-shaped particles and the second one on the pseudocubic-like particles. The ratio Fe/O for the acicular-shaped particles was 33:67, which fits perfectly well with the value of goethite, whereas for the pseudocubic-like ones, the ratio was found to be higher (38:62), which coincides with that of hematite. In this case, the Fe/O ratios cannot correspond to that calculated from the empirical formula, since ICP-MS and elemental analysis allowed obtaining an average value of the iron and hydrogen content. Therefore, EDX analysis also confirmed the presence of both phases (hematite and goethite) in agreement with XRD data.

3.2. ^{57}Fe Mössbauer spectroscopy

Mössbauer spectroscopy (MS) is a powerful technique for the characterization and quantification of iron oxides and oxyhydroxides. Mössbauer parameters can be used as "fingerprint" of iron-bearing phases and may serve to discriminate between different iron oxide and oxyhydroxide polymorphs. The Mössbauer spectra of samples Fh and H1 recorded at room temperature are depicted in Figure 2. The isomer shift is taken with respect to a bcc-Fe calibration foil measured at room temperature. Fitting of the spectra has been performed by means of the NORMOS program, developed by Brand et al.[46]

Mössbauer spectra of sample Fh, Figure 2A, showed a single paramagnetic doublet. The Mössbauer parameters for this sample are: isomer shift δ = 0.35 mm·s^{-1} and quadrupole splitting ΔE_Q = 0.62. These values are in good agreement with those reported in the literature for low ordered 2-XRD lines ferrihydrite.[47,48] Therefore, MS confirmed that sample Fh corresponds to ferrihydrite as a single phase. Mössbauer spectrum of sample H1, Figure 2B, displays a paramagnetic doublet; values of isomer shift δ = 0.35

304 mm·s^{-1} and quadrupole splitting ΔE_Q = 0.72 for this sample are consistent with the
305 presence of amorphous Fe_2O_3 consisting of very small particles, with Fe(III) ions
306 surrounded by oxygen atoms in an octahedral arrangement and symmetry axes randomly
307 oriented in a non-periodic lattice.[4,49,50]

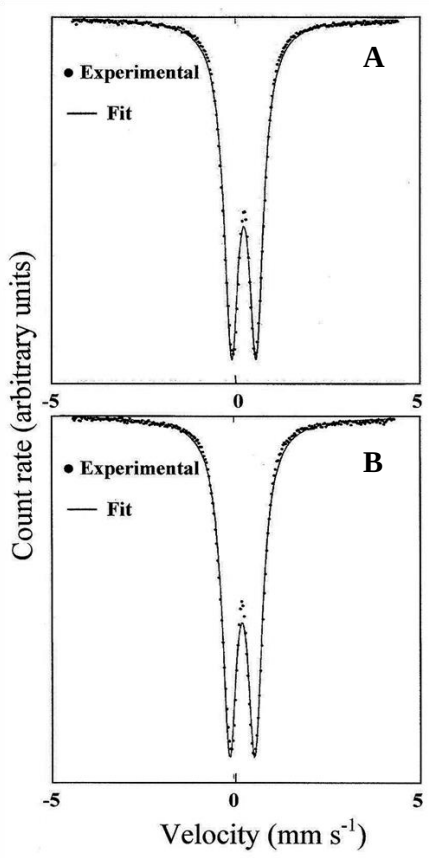

308 **Figure 2.** ^{57}Fe Mössbauer spectra recorded at RT of samples Fh (A) and H1 (B).

309 *3.3. FTIR spectroscopy*

310 Infrared (IR) spectroscopy is an extremely reliable and widely recognised
311 characterization method that allows for identification and quantification of different iron
312 oxides/oxyhydroxides. FTIR transmission spectra of the different iron samples were
313 recorded between 4000 cm^{-1} and 400 cm^{-1} and are depicted in Figure 3. The broad
314 absorption band between 3500 cm^{-1} and 3350 cm^{-1} shown in the spectrum of all of the
315 samples is attributable to OH-stretching vibrations of hydroxyls groups and water
316 molecules. The band at 1636 cm^{-1} can be assigned to hydroxyl bending vibrations. The

sharp band at 668 cm^{-1} was associated to lattice vibrations[51,52] and also appears in the spectrum of all the samples.

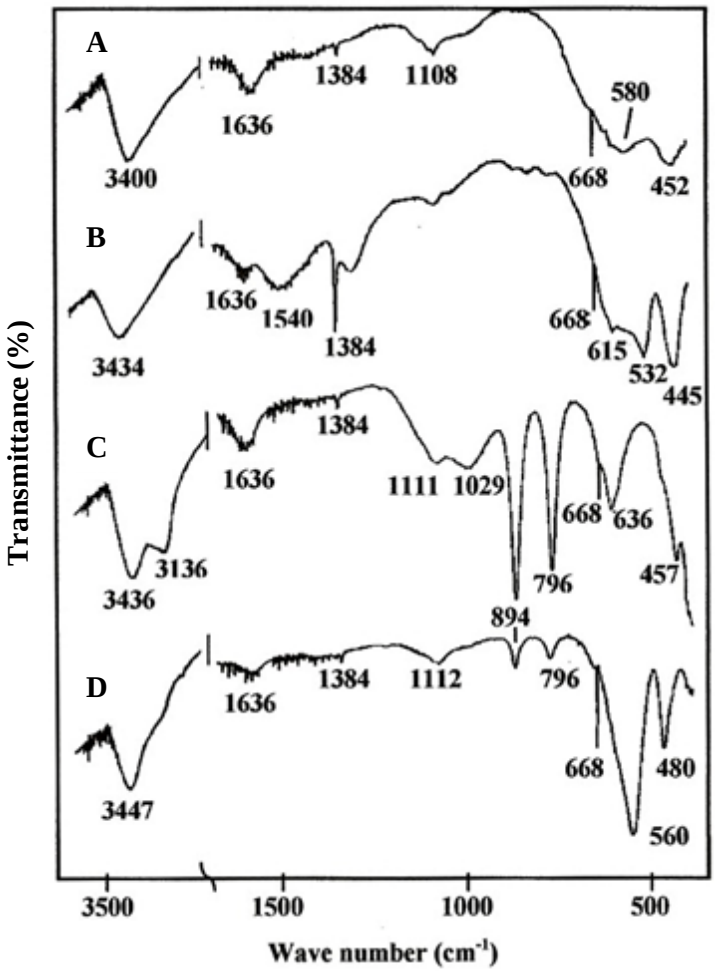

Figure 3. FTIR transmission spectra of samples Fh (A), H2 (B), G1 (C) and GH (D).

The FTIR spectrum of sample Fh, Figure 3A, appeared in the low frequency region bands centered at 580 cm^{-1} and 452 cm^{-1} that are characteristic of low ordered ferrihydrite or "amorphous" iron(III)-hydroxide.[44,47] Additional bands at 1384 and 1108 cm^{-1} can be assigned to stretching vibrations of carbonate species.[53] The presence of carbonate species in the samples, suggested by the IR bands at ~ 1540, 1384 and 1115 cm^{-1}, it is not unusual because iron(III) oxides/oxyhydroxides are susceptible to carbonation by atmospheric CO_2. The FTIR spectra of samples H1 and H2 are very similar, so only the spectrum of H2 is depicted in Figure 3B. It is worthy to note that this spectrum presents a shoulder at

615 cm^{-1} assigned to hydroxyl translation modes of adsorbed water; in the low frequency region the spectra featured two prominent peaks at 532 and 445 cm^{-1} characteristic of hematite.[54,55] The FTIR spectra of sample G1, Figure 3C, and G2 (not depicted) showed two broad absorptions at 3436 cm^{-1} and 3136 cm^{-1}. The band at 3436 cm^{-1} can be assigned to the hydroxyl stretching modes of physically adsorbed H_2O molecules or to hydrogen-bonded surface OH groups. The absorption band at 3136 cm^{-1} can be attributed to OH stretching vibrations in the goethite structure[56]; the band at 1636 cm^{-1} is due to hydroxyl bending vibrations. The strong and sharp bands at 894 and 796 cm^{-1} correspond to Fe–O–H vibrations and are characteristic of goethite. The mode at 894 cm^{-1} is assigned to in-plane deformation (δ) modes of hydroxyls and the mode at 796 cm^{-1} corresponds to out-of-plane deformation (γ) modes.[57,58] Low wavenumber modes of goethite are due to Fe-O lattice vibrations; the band at 636 cm^{-1} was attributed to FeO_6 vibration in the a plane, while the 457 cm^{-1} band was attributed to FeO_6 vibration in the b–c plane.[58] In Figure 3D is shown the spectrum of sample GH. The strong and sharp bands characteristic of goethite at 894 cm^{-1} and 796 cm^{-1} exhibited low intensity; the bands at 560 and 480 cm^{-1} can be assigned to hematite. It was reported that the IR bands at 526 and 440 cm^{-1} are the ''fingerprint'' of hematite,[55] however morphological effects can vary positions and intensity of these bands.[54] The FTIR data showed that sample GH consists of a mixture of hematite and goethite, being hematite the major crystalline phase present, which is in good agreement with the results obtained by X-ray diffraction.

3.4. Textural characterization

The surface area and the porous structure of a catalyst are fundamental features required to achieve high catalytic activity and selectivity. The effect of the synthesis procedure on the textural properties was studied from the data obtained by nitrogen

physical adsorption experiments. In Figures 4A to 4F are depicted the isotherms corresponding to the different solids, both before and after the catalytic process.

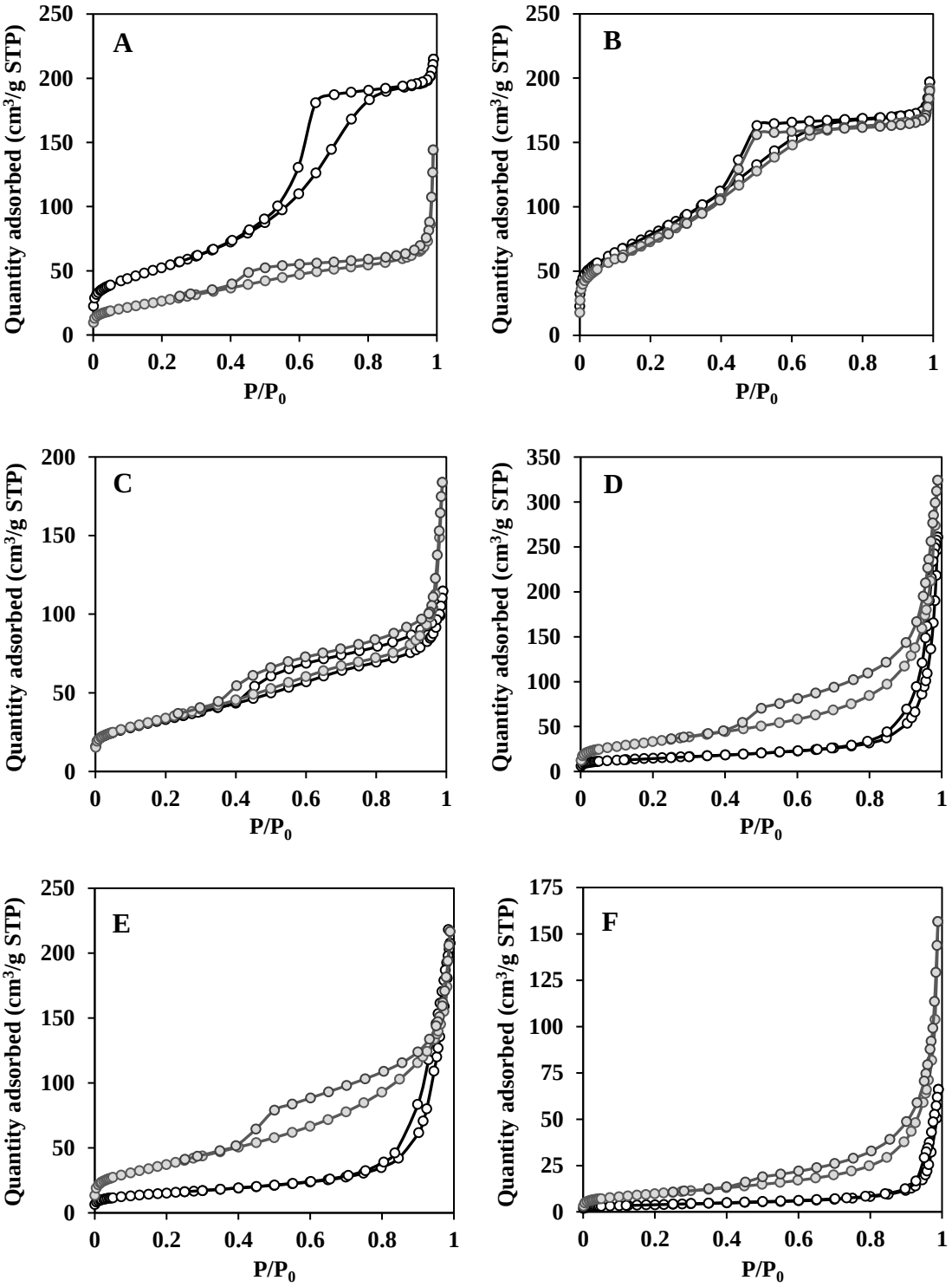

Figure 4. Nitrogen adsorption-desorption isotherms at 77 K of Fh (A), H1 (B), H2 (C), G1 (D) G2 (E) and GH (F) before (black line) and after catalytic wet oxidation (grey line).

Considering the solids before the catalytic process, it should be noted that the N_2 adsorption–desorption isotherms at 77 K belong to type IV of the BDDT classification.[59] All the isotherms presented a hysteresis loop, which is indicative of the presence of mesoporosity. The isotherm of solids H1 and Fh showed H2-type hysteresis loops, which are associated with a constricted porous networks or ink-bottle pores.[60,61] The isotherms of the rest of the solids (H2, G1, G2 and GH) presented H3-type hysteresis loop, which is related to the presence of slit-like pores.[62] Besides, all the isotherms showed a continuous nitrogen uptake at relative pressures close to 1, which reveals the presence of macroporosity in all samples. Specific surface areas were calculated using the BET equation. Mesopore volumes and pore size distributions were calculated through the method of Barrett et al.[29], applied to the adsorption and desorption branches of the isotherms. Values of the textural parameters of the solids before being employed as catalysts are given in Table 2.

Table 2. Textural parameters of iron(III) oxides and oxyhydroxides obtained from N_2 adsorption-desorption isotherms at 77 K before and after catalytic wet oxidation.

Sample	BET surface area (m^2/g)	Pore volume (cm^3/g)	Average pore diameter[a] (nm)	Average pore diameter[b](nm)
Fh	**192.3**	**0.341**	**5.54**	**5.00**
Fh*	***99.5***	***0.232***	***8.65***	***8.54***
H1	**291.4**	**0.328**	**3.97**	**3.32**
H1*	***269.3***	***0.341***	***4.18***	***3.43***
H2	**118.3**	**0.188**	**6.20**	**5.77**
H2*	***123.3***	***0.294***	***8.98***	***7.78***
G1	**51.3**	**0.404**	**32.20**	**28.36**
G1*	***120.3***	***0.507***	***15.13***	***11.46***
G2	**53.6**	**0.322**	**23.95**	**22.07**
G2*	***137.5***	***0.344***	***9.06***	***7.66***
GH	**13.2**	**0.102**	**31.56**	**27.74**
GH*	***35.4***	***0.243***	***23.84***	***18.75***

***After catalytic wet oxidation.* [a]from BJH adsorption. [b]From BJH desorption.

372 The influence of the synthesis procedure on the textural properties was studied by
373 comparing the values obtained for the textural parameters of the samples. The solids
374 obtained by the microemulsion synthetic route (Fh) and by precipitation (H1 and H2)
375 exhibited considerably higher values of BET surface area and smaller mesopore
376 diameters (Table 2); both methods led to the formation of nanostructured mesoporous
377 iron oxides.

378 Sample H1, with an XRD-pattern characteristic of a very poorly ordered material that
379 was ascribed to "amorphous" hematite nanoparticles,[37] had the highest specific surface
380 area (291.4 m^2/g) and the smallest average pore diameter (<4 nm). Supattarasakda et al.[63]
381 reported values of BET surface area (18.5-55.4 m^2/g) much lower than that obtained in
382 this study. This difference can be due to the high crystallinity of the particles of hematite
383 prepared in aforementioned study.

384 The BET surface area of low ordered 2-lines ferrihydrite (sample Fh) was also
385 considerably higher (192.3 m^2/g) than that of the samples with higher crystal order (Table
386 2), but it is ~ 34% lower than that of H1. Reported values of BET surface area, average
387 pore size and pore volume of Fh obtained by microemulsion method varied widely among
388 the different studies, ranging from 97 to 390 m^2/g, 5.6 to 9.3 nm and 0.25 to 0.54 cm^3/g,
389 respectively. All of the values obtained in this study fall within these ranges.[64,65]

390 The specific surface area of sample H2 (118.3 m^2/g) is 59% lower than that of H1;
391 calcination of H2 at 300 ºC favoured particle growth and partial welding (brought about
392 by solid-state diffusion) with formation of wider pores (Table 2). These processes would
393 account for the differences observed in the textural parameters of both samples. As will
394 be shown, the catalytic activity is clearly related to the specific surface area and the porous
395 structure of the catalysts, being the iron(III) phases with the largest surface area and
396 smallest mesopore diameter (samples H1 and Fh) considerably more active than the lower

surface area phases in the catalytic treatment of non-biodegradable landfill leachates by wet oxidation processes.

The BET surface area of samples G1 and G2 (51.3 m^2/g and 53.6 m^2/g, respectively) was considerably lower than that of samples Fh, H1 and H2. Formation of many small particles is kinetically favoured at the initial stages of the synthesis but, because larger crystals are thermodynamically more stable than smaller ones, crystal growth was favoured by the prolonged aging time in a highly alkaline medium,[51] which resulted in a reduction of the specific surface area and increased pore diameters, namely 32.20 nm for sample G1 and 23.95 nm for G2. Slow addition of the NaOH solution to the reaction mixture during the synthesis of G1 led to the formation of wider mesopores, whereas the rapid addition of the basic solution favoured yielded narrower pores, which explains the slightly higher value of the BET area of sample G2. The values of BET surface areas here determined are in the range of those reported in the literature (from 40.2 to 133.8 m^2/g)[19,66]

Sample GH exhibited the lowest BET area, 13.2 m^2/g; the XRD pattern of this sample showed diffraction peaks typical of a highly ordered solid consisting of a mixture of larger hematite and goethite crystals. Nitrogen adsorption data revealed a clear correlation between the textural properties of the iron(III) phases synthesised and the preparation procedures.

Iron(III) oxides/oxyhydroxides underwent significant textural changes during the catalytic process as demonstrated by nitrogen adsorption-desorption data. Nevertheless, the shape of the isotherms again corresponded to type IV and exhibited hysteresis loops. The values obtained for the various textural parameters are also given in Table 2. The BET surface area of sample Fh was drastically reduced from 192.3 to 99.5 m^2/g, a drop of ~52%. This reduction can be attributed to the partial transformation of ferrihydrite into highly ordered hematite.

The BET surface area of H1 was reduced by approximately 7.5%. The catalytic process favoured the formation of larger particle aggregates and slightly wider pores, which would justify the slight pore volume increase (see Table 2). The BET area of used H2 slightly rose from 118.3 m^2/g to 123.3 m^2/g (~ 4%), due to the formation of a spongier microstructure with wider mesopores. The specific surface area of the used goethite samples increased significantly, from 51.3 m^2/g to 120.3 m^2/g for sample G1, and from 53.6 to 137.5 m^2/g for G2. The porous structure of both oxyhydroxides was considerably modified during the catalytic process, the average pore diameter decreasing by ~17 nm for G1 and ~15 nm for G2. These drastic changes in the properties of samples G1 and G2 are due to the fragmentation of the acicular-shaped goethite particles during the oxidation, which resulted in the formation of porous solids made up of considerably smaller particles and narrower mesopores. The BET area of sample GH also increased greatly as well as the pore volume (Table 2). Textural changes of GH were caused by fragmentation of the goethite needles and the size reduction of the hematite particles under the catalytic process conditions.

3.5. Microstructure: SEM and TEM Microscopy

In Figures 5 and 6 are shown the SEM and TEM images of the samples before and after the catalytic oxidation process. The results obtained showed that the crystal morphology of the synthesised solids was clearly related to the different preparation procedures. At different reaction conditions, various phases may exist, because the resulting morphology of the iron(III) oxides and oxyhydroxides depends on the competition between several processes like nucleation, growth, aggregation and presence of impurities. SEM and TEM micrographs of sample Fh are displayed in Figure 5A and 5G, respectively. The SEM image obtained for 2-line ferrihydrite showed the presence of spheroidal particle aggregates, which leads to a rough surface and to the formation of a

porous structure. The image also reveals the presence of wide inter particle cavities that are probably responsible for macroporosity. Enhanced resolution was achieved with TEM microscopy, and the TEM image of sample Fh (Figure 5G) showed that the shape and size of ferrihydrite nanoparticles was quite uniform; the average particle size obtained from measurements on different particles was 7 nm. The particles are heavily aggregated appearing as clusters of small nanocrystals. This value of particle size is similar to that found in the literature for ferryhidrite prepared by microemulsion.[64]

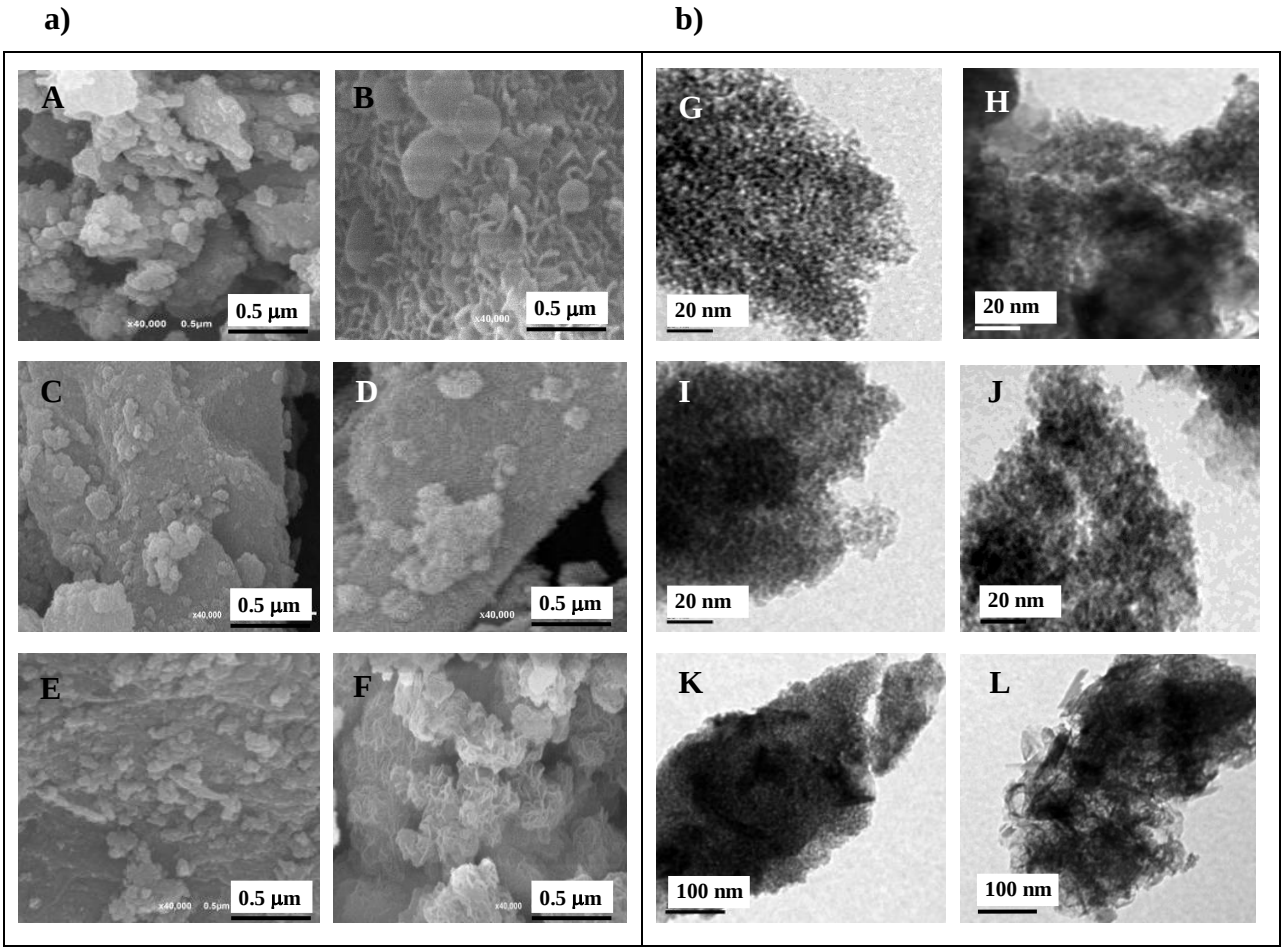

Figure 5. a) SEM images of samples before catalytic wet oxidation: Fh (A), H1 (C) and H2 (E), and after catalytic wet oxidation: Fh (B), H1 (D) and H2 (F). b) TEM images of samples before catalytic wet oxidation: Fh (G), H1 (I) and H2 (K) and after catalytic wet oxidation: Fh (H), H1 (J) and H2 (L).

458 The microstructure of Fh was drastically modified during the catalytic process. Thus, the
459 presence of hematite particles with a pseudocubic-like morphology (partial
460 transformation of ferrihydrite into hematite) was observed (see Figures 5B and 5H).

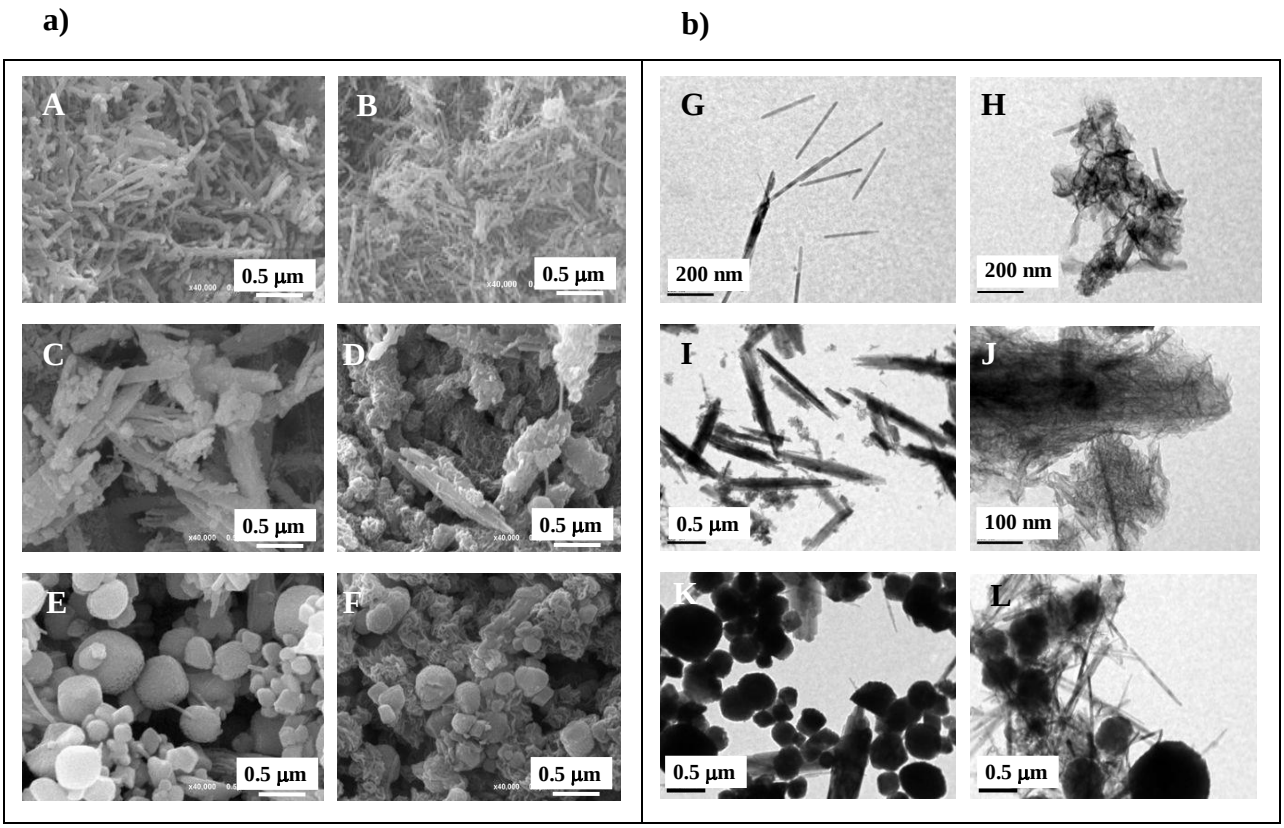

461 **Figure 6.** a) SEM images of samples before catalytic wet oxidation: G1 (A), G2 (C) and
462 GH (E), and after catalytic wet oxidation: G1 (B), G2 (D) and GH (F). b) TEM images of
463 samples before catalytic wet oxidation: G1 (G), G2 (I) and GH (K) and after catalytic wet
464 oxidation: G1 (H), G2 (J) and GH (L).

465 SEM micrographs of samples H1 and H2 (Figure 5C and 5E) showed the presence
466 of particle agglomerates with different morphology. The TEM image of sample H1
467 (Figure 5I) revealed that amorphous hematite nanoparticles had an average particle size
468 of 4 nm; particle aggregation led to the formation of a porous structure. Various authors

reported values of particle sizes between 2 and 150 nm for hematite prepared by precipitation.[63,67-69] Thus, the particle size here determined falls within this range.

The TEM micrograph of sample H2 (Figure 5K) showed that the size and shape of the hematite particles formed is heterogeneous. The presence of very fine hematite particles is responsible for the line broadening shown in the XRD-pattern of this sample; on the other hand, formation of larger hematite particles with rod-like morphology explains the drastic reduction of the BET area of this sample (59%) with respect to the specific surface area of amorphous hematite. SEM and TEM images of used H1 and H2 are shown in Figures 5D and 5J, and Figures 5F and 5L, respectively. The micrographs revealed the presence of larger particle aggregates in H1 and the evolution of the microstructure of hematite towards a spongier structure in H2.

SEM and TEM micrographs of samples G1 and G2 are shown in Figure 6A and 6G and Figure 6C and 6I, respectively. The images showed the presence of submicrometric acicular-shaped goethite particles, being bigger than those of the sample G2; the images also confirm the presence of both intra and inter particle porosity. The TEM length and width of goethite particles clearly depended on the synthesis conditions; whilst slow NaOH addition (1.5 mL/min) under gentle stirring (250 rpm) favoured the formation of smaller goethite particles (average length: 400 ± 50 nm; average width: 15 ± 5 nm), the faster addition of NaOH (3.5 mL/min) under vigorous stirring (750 rpm) favoured crystal growth, the average length and width of the resulting particles being, 950 ± 100 nm and 140 ± 20 nm, respectively. In this case, the values found in the literature varied widely. Hence, very low particles sizes (1-10 nm) were reported when goethite particles exhibited an irregular or spongy mass morphology.[70,71] However, as soon as the morphology were more defined the particle sizes increased. Thus, goethite nanotubes or nanorods showed values of average length and width from 60 to 152 nm and from 7 to 14, respectively, and

494 low acicular or rod-like goethites exhibited values of average length and width between
495 202-285 nm and 16-85 nm, respectively.[19,72-74] Besides, the length to width ratio (L/W)
496 was 26.7 and 6.98 for G1 and G2, respectively, indicating that G1 exhibited a highly
497 acicular morphology, whereas G2 is moderately acicular, according to the classification
498 of Montes-Hernandez et al.[19] Typically, the specific surface area increases with a decrease
499 in particle size, but in our study we found that sample G2, consisting of larger goethite
500 crystal, had larger specific surface than G1 (Table 2). This fact can be explained by
501 examination of the porous structure of both samples determined from N_2 adsorption-
502 desorption isotherms. The smaller value of the specific surface area of sample G1 can be
503 attributed to the presence of wider mesopores in this sample. Goethite particles of the
504 used samples G1 and G2 underwent a fragmentation process during the catalytic
505 oxidation (see Figures 6B and 6H and Figures 6D and 6J, respectively).

506 SEM and TEM micrographs of sample GH are shown in Figure 6E and Figure 6K,
507 respectively. The images showed that this sample consists of a mixture of hematite and
508 goethite particles. The major crystalline phase was made up of hematite particles of
509 different sizes (TEM average value: 170 ± 40 nm) with a pseudocubic-like morphology,
510 while submicrometric acicular-shaped goethite particles (TEM average length: 880 ± 100
511 nm; TEM average width: 145 ± 50 nm) were dispersed among the hematite particles.
512 SEM and TEM images of sample GH (Figures 6F and 6L) after its catalytic use showed
513 fragmentation of the goethite particles, as well as superficial erosion of the hematite
514 particles, which resulted in an increase of the BET area (Table 2).

515 A more detailed comparison of all these data (sections 3.1 to 3.6) with those found
516 in the literature is included in Supplementary Information (section 6).

517 *3.7. Catalytic properties of iron(III) oxides and oxyhydroxides*

518 Landfill leachates were selected as a model wastewater to assess the catalytic activity
519 of the iron(III) oxides and oxyhydroxides, due to their high content in hardly oxidisable
520 organic compounds, mainly humic and fulvic acids.[75] Hence, landfill leachates were
521 treated by catalytic wet oxidation (CWO) at 180ºC, 6.0 MPa and pH = 6.9. The operating
522 conditions were described in a previous work,[30] in which they were used for the tertiary
523 treatment of landfill leachates. The leachate employed in this work was collected from La
524 Zoreda landfill site (Asturias, Spain) and it is characterised by a very low
525 biodegradability, high values of chemical oxygen demand (COD) and a deep brown
526 colour. The composition of the leachate is described in detail in Table 3.

527 **Table 3**. Characteristics of the landfill leachate used in this work.

Parameter	Concentration
pH	6.9
COD (mg O_2/L)	1178
TOC (mg C/L)	241.1
BOD_5 (mg O_2/L)	15
Colour Number	0.625
Alkalinity (mg $CaCO_3$/L)	23.5
Conductivity (μS/cm)	13500
NH_4^+ (mg/L)	5
NO_3^- (mg/L)	673
NO_2^- (mg/L)	1
PO_4^{3-} (mg/L)	14.3

528 In Figure 7 is shown the evolution of the key parameters COD, TOC, toxicity (as
529 luminescence inhibition), biodegradability index (BOD_5/COD), and colour number (CN)
530 after 4 h and 8 h of wet oxidation treatment.

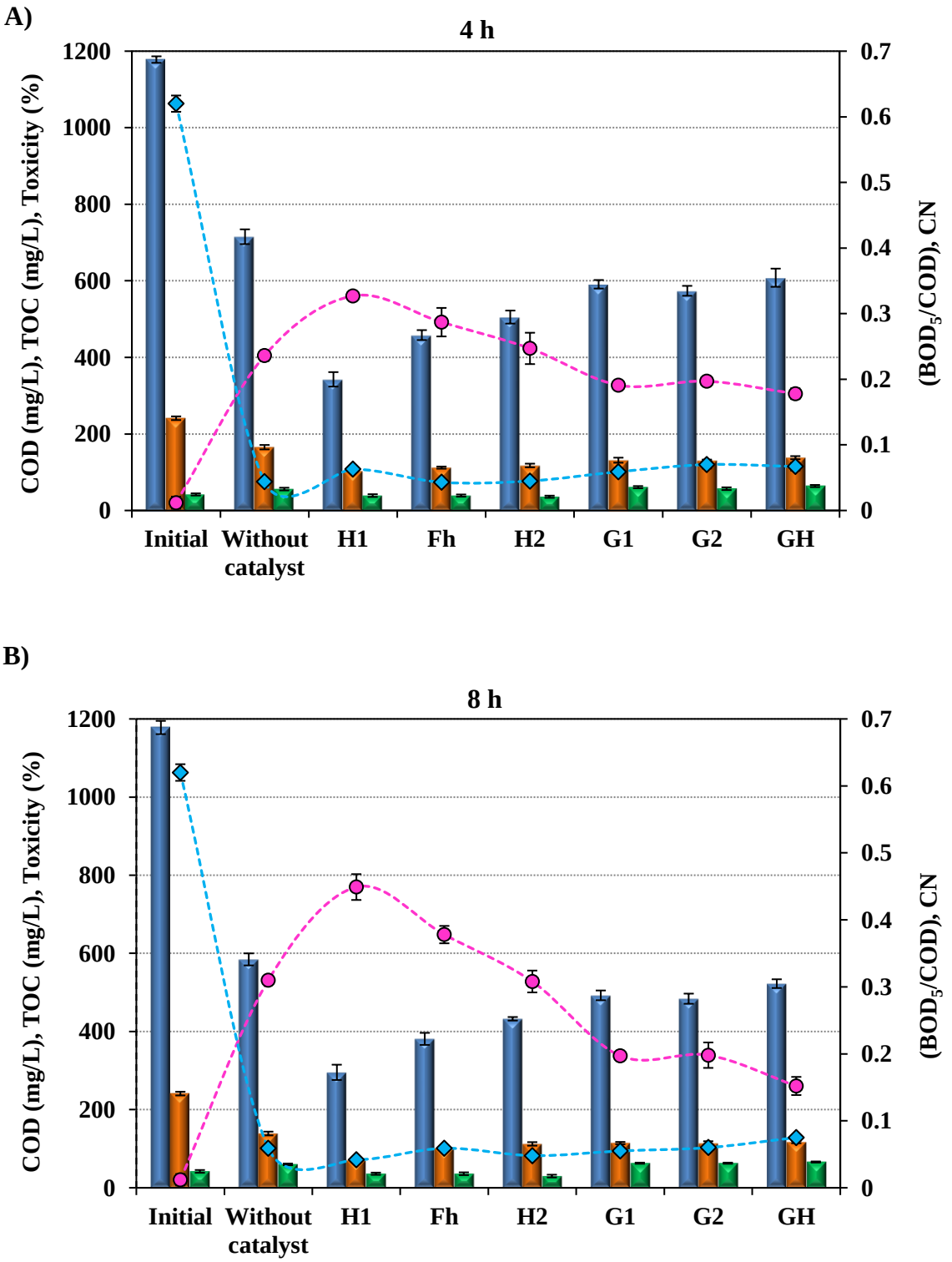

Figure 7. COD (■), TOC (■), toxicity (■), BOD_5/COD (●) and CN (◆) after 4 h (A) and 8 h (B) of wet oxidation of landfill leachates at 180ºC, 6.0 MPa and pH 6.9 in the absence and in the presence of iron oxides and oxyhydroxides as heterogeneous catalysts.

As can be seen in Figures 7A and 7B, the presence of iron catalysts has significantly improved the degree of removal of both COD and TOC, the enhancement being even more marked during the first 4 h of oxidation. In the absence of catalyst, after 4 h of non-catalytic wet oxidation, COD and TOC removals of 39% and 33% were obtained, respectively, whereas in the presence of the iron catalysts removals between 49 and 71% for COD and 43 and 64% for TOC were achieved (Figure 7A). The best catalytic results were obtained when amorphous nanostructured hematite (Sample H1) was used as heterogeneous catalyst, achieving COD and TOC removals of around 75% and 70%, respectively, after 8 h of oxidation (Figure 7B). Goi et al.[76] obtained COD removals lower than those reported in this study (40%), when landfill leachates were treated by CWO at 227ºC for 1 h employing CeO_2-SiO_2 as heterogeneous catalyst. TOC removals of 40% and 50% were achieved by Li et al. [77] when municipal landfill leachates were treated by CWO at 200ºC for 2 h using Mn/Ce oxide and Co/Bi oxide, respectively, as catalysts.

The results attained in this study proved the good catalytic performance of the iron oxides here prepared for the treatment of landfill leachates by catalytic wet oxidation. The catalytic activity of the different iron-bearing phases follows the order: H1 > Fh > H2 > G2 > G1 > GH; being the catalysts with highest BET surface area, amorphous hematite and poorly ordered 2-line ferrihydrite, the most active ones. The high activity of the low ordered phases, which exhibit a poorly defined stoichiometry, is probably due to the increased reactivity of the coordinatively unsaturated surface Fe^{3+} ions, and to the large surface area of these nanostructured solids.

Regarding the biodegradability index, BOD_5/COD, this parameter was significantly enhanced in all cases as compared to the biologically treated leachate, obtaining in the best of the cases (H1 as catalyst) a highly biodegradable leachate after 8 h of oxidation (BOD_5/COD=0.45) (Figure 7B). Besides, the colour of the treated leachate shifted from

559 dark brown to pale yellow, achieving removal rates of up to 90% (Figures 7A and 7B).
560 Bacterial toxicity of the treated effluent was slightly enhanced when CWO was performed
561 using the less active catalysts (Figure 7), however, a decrease of around 12% of the initial
562 value was achieved when the treatment was performed with the more active ones (H1,
563 H2 and Fh). Therefore, nanostructured iron(III) oxides can be effectively utilised as
564 heterogeneous catalysts for the treatment of highly contaminated leachates by means of
565 catalytic wet oxidation processes, as proven by the fact that highly bioresistant organic
566 pollutants were converted to biodegradable intermediates which can be further oxidised
567 by biological methods.

568 **4. Conclusions**

569 The impact of three different synthetic routes on the structural, textural,
570 morphological and catalytic properties of the resulting iron oxides and oxyhydroxides
571 was thoroughly investigated.

572 Precipitation and microemulsion methods led to the formation of amorphous
573 hematite (H1) and ferrihydrite (Fh), both mesoporous and nanostructured materials with
574 high surface area, 291.4 m^2/g and 192.3 m^2/g, respectively. These solids proved to be very
575 effective in the CWO of non-biodegradable landfill leachates. Another hematite (H2),
576 consisting of larger rod-shaped particles, was also obtained, although the lower surface
577 area (118.3 m^2/g) associated with the rod-like morphology conferred a lower catalytic
578 activity to this material. The sol-gel method under different preparation conditions
579 allowed for the synthesis of two iron-bearing phases: i) acicular goethite (G1 and G2)
580 made up of submicrometric particles with different main sizes, medium specific surface
581 area (51.3 m^2/g and 53.6 m^2/g) and moderate catalytic activity and ii) a mixture of
582 hematite as the main crystalline phase and goethite particles dispersed among the hematite

583 particles (GH). This solid presented a low specific surface area (13.2 m^2/g) and lower
584 catalytic activity.

585 The catalytic activity of the different iron catalysts is as follows: H1 > Fh > H2 > G2
586 > G1 > GH. The two catalysts with highest BET surface area, amorphous hematite (H1)
587 and poorly ordered 2-line ferrihydrite (Fh), presented the highest efficiencies in the CWO
588 of non-biodegradable landfill leachates, which can be attributed to the increased reactivity
589 of the coordinatively unsaturated surface Fe^{3+} ions, and to the large surface area of these
590 nanostructured solids. For instance, when H1 was used as catalyst, the removal of either
591 COD or TOC, after 4 h of oxidation, was approximately two times higher than that
592 obtained in absence of catalyst at the same reaction time. Moreover, such iron catalysts
593 were also very effective in increasing the biodegradability of the treated leachates, thus
594 obtaining effluents which ranged from moderately to highly biodegradable.

595 **Acknowledgements**

596 This work was co-financed by Spanish MINECO and FEDER funds from European
597 Union (Project CTM2012-30683). P. Oulego acknowledges an FPI grant from Spanish
598 MICINN (BES-2010-038453). Technical assistance from the Scientific-Technical
599 Services of the University of Oviedo is gratefully acknowledged. The authors particularly
600 thank Prof. José Javier Saiz and Prof. Federico Mijangos from the University of Basque
601 Country, for their assistance during Mössbauer data collection. Authors would also like
602 to thank José Manuel González and Roberto García from Consorcio para la Gestión de
603 los Residuos Sólidos en Asturias (COGERSA) for their assistance in data related to the
604 landfill leachates and for their support in the sample collection.

References

1. M. Mohapatra and S. Anand, *Int. J. Eng. Sci. Tech.*, 2010, **2**, 127-146.
2. M. Fernández-García, A. Martínez-Arias, J. C. Hanson and J. A. Rodriguez, *Chem. Rev.*, 2004, **104**, 4063-4104.
3. U. Schwertmann and R.M. Cornell, *Iron Oxides in the Laboratory: Preparation and Characterization*, 2nd ed., Wiley-VCH Verlag GMBH & Co. KGaA, Weinheim, 2000.
4. R. Zboril, M. Mashlan and D. Petridis, *Chem. Mater.*, 2002, **14**, 969-982.
5. S. Laurent, D. Forge, M. Port, A. Roch, C. Robic, L. Vander Elst and R. N. Muller, *Chem. Rev.*, 2008, **108**, 2064-2110.
6. A. K. Gupta and M. Gupta, *Biomaterials*, 2005, **26**, 3995-4021.
7. L. Xu, S. Bao, R. J. O'Brien, D. J. Houpt and B. H. Davis, *Fuel Sci. Techn. Int.*, 1994, **12**, 1323-1353.
8. E. de Smit, F. M. F. de Groot, R. Blume, M. Havecker, A. Knop-Gericke and B. M. Weckhuysen, *Phys. Chem. Chem. Phys.*, 2010, **12**, 667-680.
9. T. W. Hamann, *Dalton Trans.*, 2012, **41**, 7830-7834.
10. M.-T. Nguyen, N. Seriani and R. Gebauer, *Phys. Chem. Chem. Phys.*, 2015, **17**, 14317-14322.
11. J. Miki, M. Asanuma, Y. Tachibana and T. Shikada, *J. Catal*, 1995, **151**, 323-329.
12. N. Mimura, I. Takahara, M. Saito, T. Hattori, K. Ohkuma and M. Ando, *Catal. Today*, 1998, **45**, 61-64.
13. J. Y. T. Chan, S. Y. Ang, E. Y. Ye, M. Sullivan, J. Zhang and M. Lin, *Phys. Chem. Chem. Phys.*, 2015, **17**, 25333-25341.
14. P. Mäkie, P. Persson and L. Österlund, *J. Phys. Chem. C*, 2012, **116**, 14917-14929.
15. K.-H. Kim and S.-K. Ihm, *J. Hazard. Mater.*, 2011, **186**, 16-34.

16. J. Levec and A. Pintar, *Catal. Today*, 1995, **24**, 51-58.
17. S. K. Bhargava, J. Tardio, J. Prasad, K. Föger, D. B. Akolekar and S. C. Grocott, *Ind. Eng. Chem. Res.*, 2006, **45**, 1221-1258.
18. W. Hamd, S. Cobo, J. Fize, G. Baldinozzi, W. Schwartz, M. Reymermier, A. Pereira, M. Fontecave, V. Artero, C. Laberty-Robert and C. Sanchez, *Phys. Chem. Chem. Phys.*, 2012, **14**, 13224-13232.
19. G. Montes-Hernandez, P. Beck, F. Renard, E. Quirico, B. Lanson, R. Chiriac and N. Findling, *Cryst. Growth Des.*, 2011, **11**, 2264-2272.
20. O. Pascu, E. Carenza, M. Gich, S. Estradé, F. Peiró, G. Herranz and A. Roig, *J. Phys. Chem. C*, 2012, **116**, 15108-15116.
21. N. S. Chaudhari, S. S. Warule, S. Muduli, B. B. Kale, S. Jouen, B. Lefez, B. Hannoyer and S. B. Ogale, *Dalton Trans.*, 2011, **40**, 8003-8011.
22. Z. Kozakova, I. Kuritka, N. E. Kazantseva, V. Babayan, M. Pastorek, M. Machovsky, P. Bazantand P. Saha, *Dalton Trans.*, 2015, **44**, 21099-21108.
23. L. Guo, Q. Huang, X.-y. Li and S. Yang, *Phys. Chem. Chem. Phys.*, 2001, **3**, 1661-1665.
24. A. Bumajdad, S. Ali and A. Mathew, *J. Colloid Interf. Sci.*, 2011, **355**, 282-292.
25. M. Cheng, W. Ma, J. Li, Y. Huang, J. Zhao, Y. x. Wen and Y. Xu, *Environ. Sci. Technol.*, 2004, **38**, 1569-1575.
26. L. Geng, X. Zhang, W. Zhang, M. Jia and G. Liu, *Chem.Commun.*, 2014, **50**, 2965-2967.
27. F. Shi, M. K. Tse, M.-M. Pohl, A. Brückner, S. Zhang and M. Beller, *Angew.Chem. Int. Edit.*, 2007, **46**, 8866-8868.
28. T. Sugimoto and K. Sakata, *J. Colloid Interf. Sci.*, 1992, **152**, 587-590.
29. E. P. Barrett, L. G. Joyner and P. P. Halenda, *J. Am. Chem. Soc.*, 1951, **73**, 373-380.

30. P. Oulego, S. Collado, A. Laca and M. Díaz, *Chem. Eng., J.*, 2015, **273**, 647-655.
31. APHA, AWWA and WEF.*Standard Methods for Examination of Water and Wastewater*, 21th ed., APHA, Washington, DC, 1999.
32. ISO 11348-3, *Water Quality – Determination of the Inhibitory Effect of Water Samples on the Light Emission of Vibrio fischeri (Luminescent Bacteria Test),*International Standardization Organization, Geneva, 2007.
33. K. Rout, M. Mohapatra and S. Anand, *Dalton Trans.*, 2012, **41**, 3302-3312.
34. H. Tüysüz, E. L. Salabaş, C. Weidenthaler and F. Schüth, *J. Am. Chem. Soc.*, 2007, **130**, 280-287.
35. M. Fleischer, G. Y. Chao and A. Kato, *Am. Mineral.*, 1975, **60**, 485-489.
36. F. M. Michel, L. Ehm, S. M. Antao, P. L. Lee, P. J. Chupas, G. Liu, D. R. Strongin, M. A. A. Schoonen, B. L. Phillips and J. B. Parise, *Science*, 2007, **316**, 1726-1729.
37. P. Ayyub, M. Multani, M. Barma, V. R. Palkar and R. Vijayaraghavan, *J. Phys. C Solid State*, 1988, **21**, 2229.
38. M. Tadic, N. Citakovic, M. Panjan, B. Stanojevic, D. Markovic, Đ. Jovanovic and V. Spasojevic, *J. Alloy. Compd.*, 2012, **543**, 118-124.
39. W. Qin, C. Yang, R. Yi and G. Gao, *J. Nanomater.*, 2011, **2011**, 1-5.
40. L. Zhang, C.M.B. Holt, E.J. Luber, B.C. Olsen, H. Wang, M. Danaie, X. Cui, X. Tan, V. W. Lui, W.P. Kalisvaart, D. Mitlin, .*J. Phys. Chem. C* 2011, **115**, 24381-24393.
41. I. V. Chernyshova, S. Ponnurangam and P. Somasundaran, *Phys. Chem. Chem. Phys.*, 2010, **12**, 14045-14056.
42. M. Ristić, I. Opačak, J. Štajdohar and S. Musić, *J. Mol. Struct.*, 2015, **1090**, 129-137.
43. C. Wei, P. Qiao, Z. Nan, *Mater. Sci. Eng*: C, 2012, **32**, 1524-1530.
44. U. Schwertmann, J. Friedl, and H. Stanjek, J. Colloid Interface Sci., 1999, **209**, 215–223.

45. M. Tadic, M. Panjan, V. Damnjanovic and I. Milosevic, *Appl. Surf. Sci.*, 2014, **320**, 183-187.
46. R. A. Brand, J. Lauer and D. M. Herlach, *J. Phys. F Met. Phys.*, 1983, **13**, 675-683.
47. M. Ristić, E. De Grave, S. Musić, S. Popović and Z. Orehovec, *J. Mol. Struct.*, 2007, **834–836**, 454-460.
48. E. Murad, *Phys. Chem. Miner.*, 1996, **23**, 248-262.
49. M. Mashlan, R. Zboril, L. Machala, M. Vujtek, J. Walla and K. Nomura, *J. Metastab. Nanocryst.*, 2004, **20-21**, 641-647.
50. N. Pariona, K. I. Camacho-Aguilar, R. Ramos-González, A. I. Martinez, M. Herrera-Trejo and E. Baggio-Saitovitch, *J. Magn. Magn. Mater.*, 2016, **406**, 221-227.
51. S. Krehula and S. Musić, *J. Cryst. Growth*, 2008, **310**, 513-520.
52. P. S. R. Prasad, K. Shiva Prasad, V. Krishna Chaitanya, E. V. S. S. K. Babu, B. Sreedhar and S. Ramana Murthy, *J. Asian Earth Sci.*, 2006, **27**, 503-511.
53. C. Su and D. L. Suarez, *Clay. Clay. Miner.*, 1997, **45**, 814-825.
54. J. E. Iglesias, C.J. Serna, *Miner. Petrogr. Acta* 1985,***29A***, 363-370.
55. A. M. Jubb and H. C. Allen, *ACS Appl. Mater. Inter.*, 2010, **2**, 2804-2812.
56. M. Gotić and S. Musić, *J. Mol. Struct.*, 2007, **834–836**, 445-453.
57. H. D. Ruan, R. L. Frost and J. T. Kloprogge, *Spectrochim. Acta A*, 2001, **57**, 2575-2586.
58. J. D. Russell and A. R. Fraser, in *Clay Mineralogy: Spectroscopic and Chemical Determinative Methods*, ed. M. J. Wilson, Springer Netherlands, Dordrecht, 1994, pp. 11-67.
59. S. Brunauer, L. S. Deming, W. E. Deming and E. Teller, *J. Am. Chem. Soc.*, 1940, **62**, 1723-1732.

60. C. Sangwichien, G. L. Aranovich and M. D. Donohue, *Colloid. Surface. A*, 2002, **206**, 313-320.
61. K. S. W. Sing, D. H. Everett, R. A. W. Haul, L. Moscou, R. A. Pierotti, J. Rouquérol and T. Siemieniewska, *Pure Appl. Chem.*, 1985, **57**, 603-619.
62. F. Mou, J. Guan, Z. Xiao, Z. Sun, W. Shi and X.-a. Fan, *J. Mater. Chem.*, 2011, **21**, 5414-5421.
63. K. Supattarasakda, K. Petcharoen, T. Permpool, A. Sirivat and W. Lerdwijitjarud, *Powder Technol.*, 2013, **249**, 353-359.
64. Z. Yan, Z. Xu, J. Yu and M. Jaroniec, *Environ. Sci. Technol.*, 2015, **49**, 6637-6644.
65. Z. Xu, J. Yu and W. Xiao, *Chem – Eur. J.*, 2013, **19**, 9592-9598.
66. M. Kosmulski, E. Maczka, E. Jartych and J. B. Rosenholm, *Adv. Colloid Interfac.*, 2003, **103**, 57-76.
67. B. Paul, B. Bhuyan, D. D. Purkayastha and S. S. Dhar, *Catal. Commun.*, 2015, **69**, 48-54.
68. S. Sivakumar, D. Anusuya, C. P. Khatiwada, J. Sivasubramanian, A. Venkatesan and P. Soundhirarajan, *Spectrochim. Acta Part A*, 2014, **128**, 69-75.
69. H. Liu, Y. Wei, P. Li, Y. Zhang and Y. Sun, *Mater. Chem. Phys.*, 2007, **102**, 1-6.
70. M. Mohapatra, K. Rout, S. K. Gupta, P. Singh, S. Anand and B. K. Mishra, *J. Nanopart. Res.*, 2009, **12**, 681-686.
71. D. N. Bakoyannakis, E. A. Deliyanni, A. I. Zouboulis, K. A. Matis, L. Nalbandian and T. Kehagias, *Micropor. and Mesopor. Mat.*, 2003, **59**, 35-42.
72. T. Yu, J. Park, J. Moon, K. An, Y. Piao and T. Hyeon, *J. Am. Chem. Soc.*, 2007, **129**, 14558-14559.
73. D. M. E. Thies-Weesie, J. P. de Hoog, M. H. Hernandez Mendiola, A. V. Petukhov and G. J. Vroege, *Chem. Mater.*, 2007, **19**, 5538-5546.

74. R. Lee Penn, J. J. Erbs and D. M. Gulliver, *J. Cryst. Growth*, 2006, **293**, 1-4.

75. T. A. Kurniawan, W. Lo, G. Chan and M. E. T. Sillanpaa, *J. Environ. Monitor*., 2010, **12**, 2032-2047

76. D. Goi, C. d. Leitenburg, G. Dolcetti and A. Trovarelli, *J. Alloy. Compd.*, 2006, **408–412**, 1136-1140.

77. Y. Li, J. Wang, Y. Liu, *IEEE* 2008, 3048-3050.

Supplementary Information to

'Effect of the synthetic route on the structural, textural, morphological and catalytic properties of Iron(III) oxides and oxyhydroxides'

Paula Oulego[a], María A. Villa-García[b], Adriana Laca [a]and Mario Diaz[a]*

[a]Department of Chemical and Environmental Engineering, University of Oviedo.

[b]Department of Organic and Inorganic Chemistry, University of Oviedo.

c/Julián Clavería, s/n, 33071, Oviedo, Spain

(29 Pages, 5 Tables, 2 Figures)

Table of contents

*Corresponding author's e-mail: mavg@uniovi.es (M.A. Villa-García)
Phone: +34 985 10 29 76; Fax: +34 985 10 34 46

1. Instrumental parameters for the determination of the iron content by ICP-MS (Table S1).

Table S1. Instrumental parameters for ICP-MS.

Inductively Coupled Plasma		Mass Spectrometer	
RF power (W)	1500	Sampling cone	Nickel
Carrier gas (L/min)	1.12	Skimmer cone	Nickel
Plasma gas (L/min)	15	Data acquisition	3 points per mass
Auxiliary gas (L/min)	1.0	Integration time	0.1 s per point
Sample depth (mm)	8	Acquisitions	5
Solution uptake rate (mL/min)	0.4	Analytical masses	^{57}Fe and ^{103}Rh
Nebulizer	Babington type		

2. Determination of bacterial toxicity of the landfill leachate treated by catalytic wet oxidation

The assessment of bacterial toxicity was carried out with *Vibrio fischeri*. The commercial assay Biofix®Lumi-10 (Macherey-Nagel, Germany) was employed using a freeze-dried specially selected strain of the marine bacterium (NRRL number B-11177). Toxicity was evaluated in samples diluted 1:5 and results were given as inhibition percentage (LI) according to ISO 11348-3. The drop in light emission of the bacteria after a contact period of 15 min was measured and compared with a sample of control free of toxicants (2% NaCl solution). Temperature was kept at 15 ºC by a thermo block and sample salinity was adjusted to 2% after adjusting the sample pH between 6.5 and 7.5.

3. Determination of the color number (CN) of the landfill leachate treated by catalytic wet oxidation

As it was previously commented in the manuscript, the color number (CN), was employed to monitor changes in the color of the leachate during its oxidation, its value was calculated using equation S1. Spectral absorbance coefficients (SAC) are defined as the ratio of the values of the respective absorbance (Abs) over the cell thickness (x) (see equation S2). This parameter was measured at 436, 525 and 620 nm using a UV/Vis spectrophotometer (Thermo Scientific, Heλios γ).

$$CN = \frac{SAC_{436}^2 + SAC_{525}^2 + SAC_{620}^2}{SAC_{436} + SAC_{525} + SAC_{620}} \quad \text{(S1)}$$

$$SAC_i = \frac{Abs_i}{x} \quad \text{(S2)}$$

4. Selected electron diffraction pattern (SAED) of hematite H1 (Figure S1).

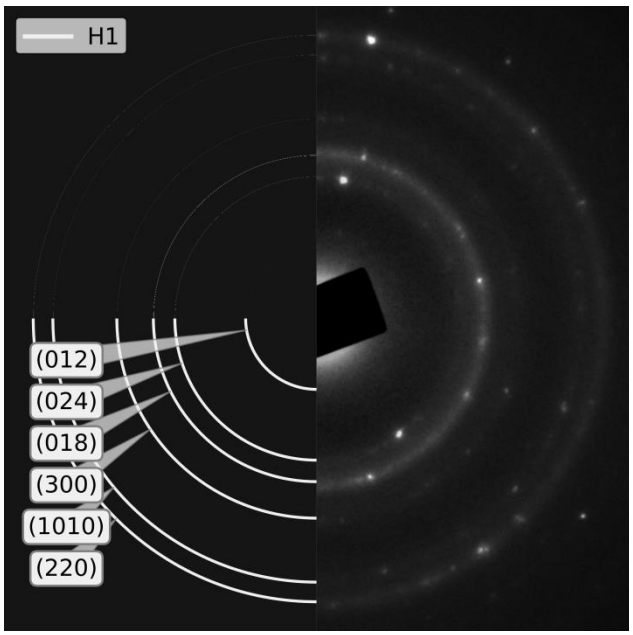

Figure S1. Electron diffraction pattern of hematite H1 (right) and simulated electron diffraction pattern of the rhomboedral hematite JCPDS no. 33-0664 (left).

5. EDX analysis of the iron(III) oxides and oxyhydroxides (Figure S2).

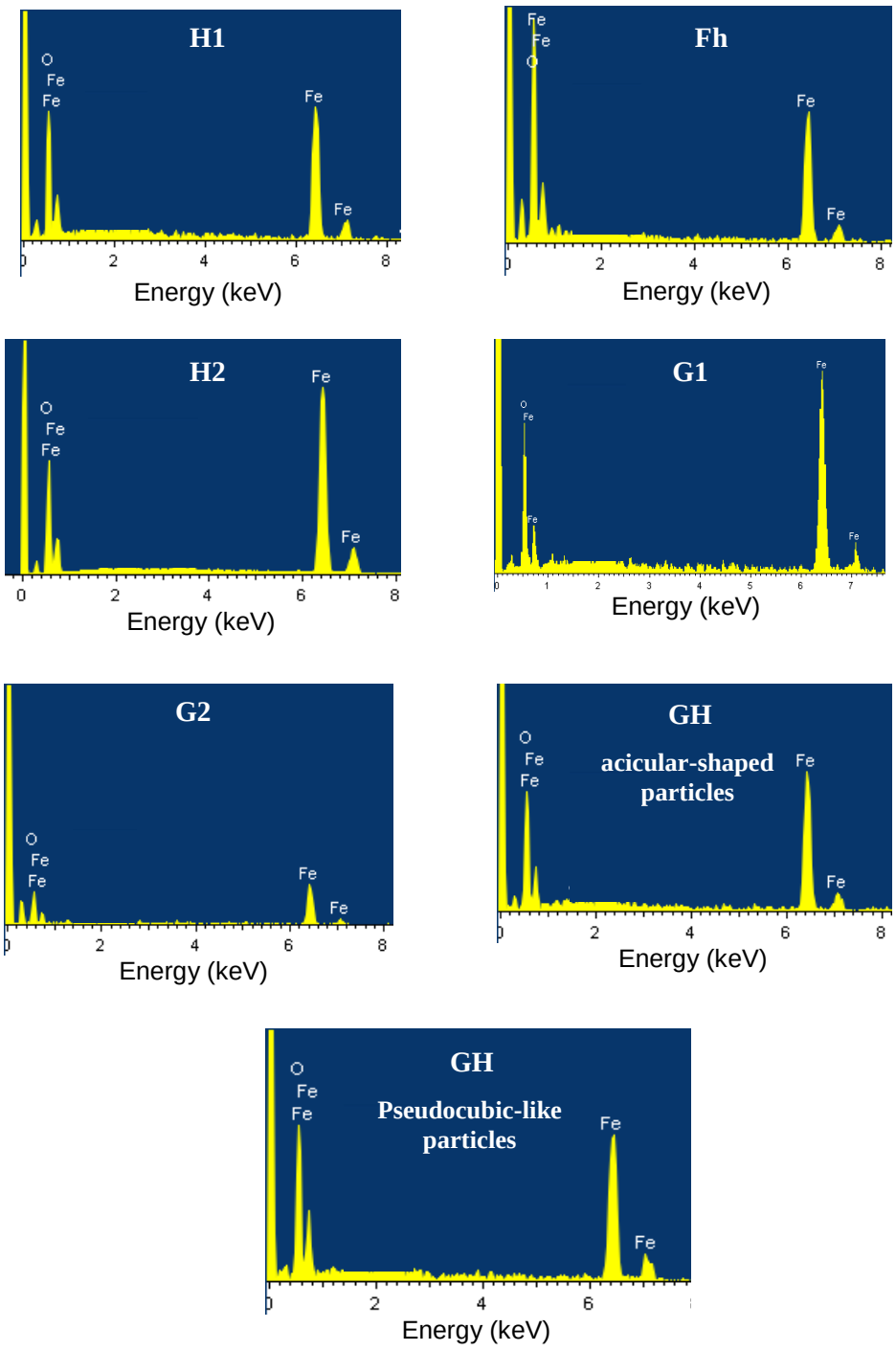

Figure S2. EDX analysis of the iron(III) oxides and oxyhydroxides.

6. Comparison of the data of this study with those found in the literature (Table S2 to S5).

Table S2. Comparison of X-ray diffraction data obtained in this study with those found in the literature.

	Results of this study				***Data found in the literature***			
Sample	***XRD peaks of the solids***	***Miller indices (hkl)***	***Iron-bearing phase***	***Crystallinity of the solids of this study***	***Miller indices (hkl)***	***Iron-bearing phase***	***Crystallinity of the solids of this study***	***Reference***
Hematite	Solid H1: 24.1º, 35.7º, 49.5º, 57.8º, 62.6º, 72.1º and 75.4º	Solid H1: (012), (110), (024), (018), (300), (1010), (220)	Rhombohedral hematite: JCPDS no. 33-0664.	Very poorly ordered material.	• Hematite nanospheres[1]: (012), (104), (110), (113), (024), (116), (018), (214), (300) • Hematite nanocubes[2] and thin film[3]: (012), (104), (110), (113), (024), (116), (018), (214), (300), (1010) • Hematite nanocubes[4]: (012), (104), (110), (006), (113), (200), (024), (116), (018), (214), (300), (208)	Rhombohedral hematite: JCPDS no. 33-0664.	• Hematite nanospheres[1]: crystalline. • Hematite nanocubes[2,4]: highly crystalline. • Hematite thin film[3]: crystalline.	[1]Tadic et al., 2012; [2]Qin et al., 2011; [3]Hamd et al., 2012; [4]Chernysho-va et al., 2010.

Table S2. Comparison of X-ray diffraction data obtained in this study with those found in the literature (continuation).

	Results of this study				***Data found in the literature***			
Sample	***XRD peaks of the solids***	***Miller indices (hkl)***	***Iron-bearing phase***	***Crystallinity of the solids of this study***	***Miller indices (hkl)***	***Iron-bearing phase***	***Crystallinity of the solids of this study***	***Reference***
Hematite	Solid H2: 24.1º, 33.4º, 35.7º, 41.1º, 49.5º, 54.2º, 62.6º, 64.1º, 72.1º and 75.4º	Solid H2: (012), (104), (110), (113), (024), (116), (214), (300), (1010), (220)	Rhombohedral hematite: JCPDS no. 33-0664.	Poorly ordered material and/or presence of very fine hematite particles	• Hematite nanospheres[1]: (012), (104), (110), (113), (024), (116), (018), (214), (300) • Hematite nanocubes[2] and thin film[3]: (012), (104), (110), (113), (024), (116), (018), (214), (300), (1010) • Hematite nanocubes[4]: (012), (104), (110), (006), (113), (200), (024), (116), (018), (214), (300), (208)	Rhombohedral hematite: JCPDS no. 33-0664.	• Hematite nanospheres[1]: crystalline. • Hematite nanocubes[2,4]: highly. crystalline • Hematite thin film[3]: crystalline.	[1]Tadic et al., 2012; [2]Qin et al., 2011; [3]Hamd et al., 2012; [4]Chernysho-va et al., 2010.

Table S2. Comparison of X-ray diffraction data obtained in this study with those found in the literature (continuation).

	Results of this study				***Data found in the literature***			
Sample	***XRD peaks of the solids***	***Miller indices (hkl)***	***Iron-bearing phase***	***Crystallinity of the solids of this study***	***Miller indices (hkl)***	***Iron-bearing phase***	***Crystallinity of the solids of this study***	***Reference***
Ferrihy-drite	Solid Fh:35.7º and 63.5º	Solid Fh: (110), (300)	No single formula is widely accepted. $Fe_{10.4}O_{14.2}(OH)_2$	Poorly ordered material.	• 2-line ferrihydrite[5,6]: (110), (300)	$Fe_{10}O_{14}(OH)_2$[5] $Fe_5HO_8 \cdot 4H_2O$[6]; $5Fe_2O_3 \cdot 9H_2O$[6,7];	Poorly crystalline.[5-7]	[5]Michel et al., 2007; [6]Tüysüz et al., 2011; [7]Fleischer et al., 1975.

Table S2. Comparison of X-ray diffraction data obtained in this study with those found in the literature (continuation).

	Results of this study				***Data found in the literature***			
Sample	***XRD peaks of the solids***	***Miller indices (hkl)***	***Iron-bearing phase***	***Crystallinity of the solids of this study***	***Miller indices (hkl)***	***Iron-bearing phase***	***Crystallinity of the solids of this study***	***Reference***
Goethite	Solid G1: 17.9º, 21.2º, 26.1º,33.2º, 33.5º, 36.7º, 40.3º, 41.4º, 45.5º, 47.6º, 50.9, 53.1º, 57.6º, 59.1º, 61.5º, 64.7º, 69.3º, 71.7º and 75.4º	Solid G1: (020), (110), (120), (130), (021), (111), (121), (140), (131), (041), (211), (221), (231), (151), (002), (061), (112), (170), (132)	Orthorhombic phase of goethite: JCPDS no. 29-0713.	Highly crystalline.	• Goethite rods[8,9]: (020), (110), (120), (130), (021), (040), (111), (200), (121), (140), (211), (221), (240), (231), (151), (160), (020), (161) • Acicular goethite[10]: (020), (110), (120), (130), (021), (040), (111), (200), (121), (140), (211), (221)	Orthorhombic phase of goethite: JCPDS no. 29-0713.	Goethite rods: highly crystalline.[8,9] Acicular goethite: highly crystalline.[10]	[8]Ristić et al., 2015; [9]Wei et al., 2012; [10]Montes-Hernandez et al., 2011.

Table S2. Comparison of X-ray diffraction data obtained in this study with those found in the literature (continuation).

	Results of this study				***Data found in the literature***			
Sample	***XRD peaks of the solids***	***Miller indices (hkl)***	***Iron-bearing phase***	***Crystallinity of the solids of this study***	***Miller indices (hkl)***	***Iron-bearing phase***	***Crystallinity of the solids of this study***	***Reference***
Goethite	Solid G2: 17.9º, 21.2º, 26.1º,33.2º, 33.5º, 36.7º, 40.3º, 41.4º, 47.6º, 50.9, 53.1º, 57.6º, 59.1º, 61.5º, 64.7º, 69.3º, 71.7º and 75.4º	Solid G2: (020), (110), (120), (130), (021), (111), (121), (140), (041), (211), (221), (231), (151), (002), (061), (112), (170), (132)	Orthorhombic phase of goethite: JCPDS no. 29-0713.	Highly crystalline	• Goethite rods[8,9]: (020), (110), (120), (130), (021), (040), (111), (200), (121), (140), (211), (221), (240), (231), (151), (160), (020), (161) • Acicular goethite[10]: (020), (110), (120), (130), (021), (040), (111), (200), (121), (140), (211), (221)	Orthorhombic phase of goethite: JCPDS no. 29-0713.	Goethite rods: highly crystalline.[8,9] Acicular goethite: highly crystalline.[10]	[8]Ristić et al., 2015; [9]Wei et al., 2012; [10]Montes-Hernandez et al., 2011.

Table S2. Comparison of X-ray diffraction data obtained in this study with those found in the literature (continuation).

	Results of this study				***Data found in the literature***			
Sample	***XRD peaks of the solids***	***Miller indices (hkl)***	***Iron-bearing phase***	***Crystallinity of the solids of this study***	***Miller indices (hkl)***	***Iron-bearing phase***	***Crystallinity of the solids of this study***	***Reference***
Mixture of hematite and goethite	Solid GH: • Hematite: 24.1º, 33.4º, 35.7º, 41.1º, 49.5º, 54.2º, 62.6º, 64.1º, 72.1º and 75.4º • Goethite: 36.7º, 53.3º, 57.6º and 59.2º	Solid GH: • Hematite: (012), (104), (110), (113), (024), (116), (214), (300), (1010), (220) • Goethite: (111), (221), (231), (151)	• Rhombohedral hematite: JCPDS no. 33-0664. • Orthorhombic phase of goethite: JCPDS no. 29-0713.	Both phases highly crystalline	• Hematite nanocubes[4] (012), (104), (110), (113), (024), (116), (018), (214), (300), (1010) • Goethite rods[8,9] (020), (110), (120), (130), (021), (040), (111), (200), (121), (140), (211), (221), (240), (231), (151), (160), (020), (161)	• Rhombohedral hematite: JCPDS no. 33-0664. • Orthorhombic phase of goethite: JCPDS no. 29-0713.	• Hematite nanocubes[4]: highly crystalline. • Goethite rods: highly crystalline.[8,9]	[4]Chernyshova et al., 2010. [8]Ristić et al., 2015; [9]Wei et al., 2012.

Table S3. Comparison of Mössbauer data obtained in this study with those found in the literature.

	Results of this study			***Data found in the literature***			
Sample	***Doublet***	***Isomer shift (***δ) mm·s^{-1}	***Quadrupole splitting (***ΔE_Q)	***Doublet***	***Isomer shift (***δ) mm·s^{-1}	***Quadrupole splitting (***ΔE_Q)	***Reference***
Ferrihydrite (Fh)	Single Paramagnetic	0.35	0.62	Paramagnetic	0.33[11] 0.35[12]	0.62[11] 0.63[12]	[11]Ristić et al., 2007; [12]Murad, 1996.
Hematite (H1)	Paramagnetic	0.35	0.72	Paramagnetic	0.35[13] 0.33[14] 0.33-0.35[15]	0.68[13] 0.75[14] 0.80[15]	[13]Pariona et al., 2016; [14]Mashlan et al., 2004; [15]Zboril et al., 2002.

Table S4. Comparison of FT-IR data obtained in this study with those found in the literature.

	Results of this study					***Data found in the literature***					
Sample	***OH stretching vibrations (cm^{-1})***	***OH bending vibrations (cm^{-1})***	***Lattice vibrations (cm^{-1})***	***Carbonate species stretching vibrations (cm^{-1})***	***Characteristic vibrations (cm^{-1})***	***OH stretching vibrations (cm^{-1})***	***OH bending vibrations (cm^{-1})***	***Lattice vibrations (cm^{-1})***	***Carbonate species stretching vibrations (cm^{-1})***	***Characte-ristic vibrations (cm^{-1})***	***Reference***
Ferrihy-drite (Fh)	3400	1636	668	1384, 1108	580, 452	3420-3357[11]	1623-1620[11]	660[11] <700[16]	1352[11] 1360[17], 1070[17]	580, 441[11]	[11]Ristić et al., 2007; [16]Krehula and Musić, 2008; [17]Su and Suarez,1997
Hematite (H1 and H2)	3434	1636	668	1540 1384	532, 445	3420-3357[11]	1623-1620[11]	660[11]	1490[17], 1360[17]	526,440[18]	[11]Ristić et al., 2007; [16]Krehula and Musić, 2008 [17]Su and Suarez, 1997; [18]Jubb et al., 2010

Table S4. Comparison of FT-IR data obtained in this study with those found in the literature (continuation).

	Results of this study					***Data found in the literature***					
Sample	***OH stretching vibrations (cm^{-1})***	***OH bending vibrations (cm^{-1})***	***Lattice vibrations (cm^{-1})***	***Carbonate species stretching vibrations (cm^{-1})***	***Characteristic vibrations (cm^{-1})***	***OH stretching vibrations (cm^{-1})***	***OH bending vibrations (cm^{-1})***	***Lattice vibrations (cm^{-1})***	***Carbonate species stretching vibrations (cm^{-1})***	***Characte-ristic vibrations (cm^{-1})***	***Reference***
Goethite (G1 and G2)	3434[a], 3136[b]	1636	668	1384, 1111	894[c], 796[d], 636[e], 457[f]	3420-3357[a,11] 3144[b,18]	1620-1623[11]	660[11] <700[16]	1352[11] 1360[17], 1070[17]	895-884[c,19,20], 800-798[d,19,20] 622-617[e,20] 461-454[f,20]	[11]Ristić et al., 2007; [16]Krehula and Musić, 2008; [17]Su and Suarez,1997; [18]Jubb et al., 2010; [19]Gotić and Musić, 2007; [20]Ruan et al., 2001.

[a]Physically adsorbed water molecules; [b]in the goethite structure; [c]Fe-O-H vibration in-plane; [d]Fe-O-H vibration out-of-plane; [e]FeO_6 vibration in the a-plane; [f]FeO_6 vibration in the b-c-plane.

Table S4. Comparison of FT-IR data obtained in this study with those found in the literature (continuation).

	Results of this study					***Data found in the literature***					
Sample	***OH stretching vibrations (cm^{-1})***	***OH bending vibrations (cm^{-1})***	***Lattice vibrations (cm^{-1})***	***Carbonate species stretching vibrations (cm^{-1})***	***Characteristic vibrations (cm^{-1})***	***OH stretching vibrations (cm^{-1})***	***OH bending vibrations (cm^{-1})***	***Lattice vibrations (cm^{-1})***	***Carbonate species stretching vibrations (cm^{-1})***	***Characte-ristic vibrations (cm^{-1})***	***Reference***
Mixture of hematite and goethite (GH)	3447	1636	668	1384, 1112	894[a], 796[b], 560[c], 480[c]	3420-3357[11]	1620-1623[11]	660[11] <700[16]	1352[11] 1360[17], 1070[17]	895-884[a,19,20], 800-798[b,19,20], 580[c,11], 441[c,11]	[11]Ristić et al., 2007; [16]Krehula and Musić, 2008; [17]Su and Suarez,1997; [19]Gotić and Musić, 2007; [20]Ruan et al., 2001.

[a]Fe-O-H vibration in-plane; [b]Fe-O-H vibration out-of-plane; [c]Bands which are the fingerprint of hematite (morphological effects can vary the positions of these bands).

Table S5. Comparison of textural characterization and microstructure of the solids obtained in this study with those found in the literature.

	Synthetic route[a]					***Data found in the literature***					
Sample	***Iron source[b]; Additive[c]***	***Method[d]***	***pH***	***T of ageing (ºC)***	***Time (h)***	***BET surface area (m^2/g)***	***Average pore size (nm)***	***Pore Volume (cm^3/g)***	***Particle Size: TEM(nm)***	***Morphology***	***Reference***
Hematite	Fe(III) salt; No additive	Precipitation	n.a.	20	4	n.a.	n.a.	n.a.	Average: 50-100	Irregular	[21]Paul et al., 2015
Hematite	Fe(III) salt; With additives	Precipitation	n.a.	20	4	244.8 - 276.2	8.83-9.74	0.596 - 0.609	Average:2-50	Quasi spherical	[21]Paul et al., 2015

[a]Implying batch system. [b]Fe(III) salt: $Fe(NO_3)_3 \cdot 9H_2O$. [c]Additives: *PEG 400 or PEG 4000*. [d]Precipitating agent: $(CH_2)_6N_4$
n.a.: Not reported.

Table S5. Comparison of textural characterization and microstructure of the solids obtained in this study with those found in the literature (continuation).

	Synthetic route[a]					***Data found in the literature***					
Sample	***Iron source[b]; Additive***	***Method[c]***	***pH***	***T of ageing (ºC)***	***Time (h)***	***BET surface area (m^2/g)***	***Average pore size (nm)***	***Pore Volume (cm^3/g)***	***Particle Size: TEM [d] or Scherrer [e] (nm)***	***Morphology***	***Reference***
Hematite	Fe(III) salt; No additive	Precipitation	n.a.	20	4	n.a.	n.a.	n.a.	Average [e]: 31	Spheroidal	[22]Sivakumar et al., 2014
Hematite	Fe(III) salt; No additive	Precipitation (under pure N_2 gas)	7	>100	1	18.5-55.4	n.a.	n.a.	Average [d]: 50-150	Spherical, cubic and ellipsoidal	[23]Supatta-rasakda et al., 2013

[a]Implying batch system. [b]Fe(III) salt: $FeCl_3 \cdot 6H_2O$. [c]Precipitating agent: NaOH
n.a.: Not reported.

Table S5. Comparison of textural characterization and microstructure of the solids obtained in this study with those found in the literature (continuation).

	Synthetic route[a]					***Data found in the literature***					
Sample	***Iron source[b]; Additive***	***Method[c]***	***pH***	***T of ageing (ºC)***	***Time (h)***	***BET surface area (m^2/g)***	***Average pore size (nm)***	***Pore Volume (cm^3/g)***	***Particle Size: TEM (nm)***	***Morphology***	***Reference***
Hematite	Fe(III) salt; No additive	Precipitation	7	>100	n.a.	17.18-31.83	n.a.	n.a.	Average: 60-80	Quasi-spherical	[24]Liu et al., 2007
Hematite	Fe(III) salt; No additive	Precipitation	H1: 9	H1: 20	H1:3	H1: 291.4	H1: 3.32-3.97	H1:0.328	H1(average): 4	H1: Spheroidal	This study
			H2: 12	H2: 20	H2:3	H2: 118.3	H2: 5.77-6.20	H2:0.188	H2: widely variable	H2: amorphous	

[a]Implying batch system. [b]Fe(III) salt: $FeCl_3 \cdot 6H_2O$ or $Fe(NO_3)_3 \cdot 9H_2O$. [c]Precipitating agent: NaOH or NH_4OH
n.a.: Not reported.

Table S5. Comparison of textural characterization and microstructure of the solids obtained in this study with those found in the literature (continuation).

	Synthetic route[a]					***Data found in the literature***					
Sample	***Iron source[b]; Additive***	***Method***	***pH***	***T of ageing (ºC)***	***Time (h)***	***BET surface area (m^2/g)***	***Average pore size (nm)***	***Pore Volume (cm^3/g)***	***Particle Size: TEM (nm)***	***Morphology***	***Reference***
Ferrihy-drite	Fe(III) salt; cyclohexane, polyethylene-glycol, ammonia solution and isopropanol	Micro-emulsion	n.a.	50	3	390	5.6	0.54	n.a.	n.a.	[25]Xu et al., 2013
Ferrihy-drite	Fe(III) salt; cyclohexane, polyethylene-glycol, ammonia solution and isopropanol	Micro-emulsion	n.a.	50	3	97	9.3	0.25	Average : 10	spherical	[26]Yan et al., 2015

[a]Implying batch system. [b]Fe(III) salt: $FeCl_3$.
n.a.: Not reported.

Table S5. Comparison of textural characterization and microstructure of the solids obtained in this study with those found in the literature (continuation).

	Synthetic route[a]					***Data found in the literature***					
Sample	***Iron source[b]; Additive***	***Method***	***pH***	***T of ageing (ºC)***	***Time (h)***	***BET surface area (m^2/g)***	***Average pore size (nm)***	***Pore Volume (cm^3/g)***	***Particle Size: TEM (nm)***	***Morphology***	***Reference***
Ferrihy-drite	Fe(III) salt; brij 58, isopropyl alcohol and ammonia solution	Micro-emulsion	8	55	72	192.3	5.00-5.54	0.341	Average: 7	Spheroidal	This study (solid Fh)

[a]Implying batch system. [b]Fe(III) salt: $Fe(NO_3)_3 \cdot 9H_2O$.

Table S5. Comparison of textural characterization and microstructure of the solids obtained in this study with those found in the literature (continuation).

	Synthetic route[a]					***Data found in the literature***					
Sample	***Iron source[b]; Additive[c]***	***Method[d]***	***pH***	***T of ageing (ºC)***	***Time (h)***	***BET surface area (m^2/g)***	***Average pore size (nm)***	***Pore Volume (cm^3/g)***	***Particle Size: FESEM [e]or TEM [f] (nm)***	***Morphology***	***Reference***
Goethite	Fe(III) salt; No additive	Sol-gel	2.5-13.5	30	24	133.80	n.a.	n.a.	Length[e]: 250±35 Width[e]: 65±20	low acicular	[10]Montes-Hernández et al., 2011
Goethite	Fe(III) salt; With additive	Sol-gel	3.0	90	1	n.a.	n.a.	n.a.	Largest dimension [f]: 1-10	Irregular	[27]Mohapatra et al., 2009

[a]Implying batch system. [b]Fe(III) salt: $Fe(NO_3)_3 \cdot 9H_2O$ or $FeCl_3 \cdot 6H_2O$ [c]Additive: hydrazine sulphate. [d]Alkaline source: NaOH or $Ca(OH)_2$.
n.a.: Not reported.

Table S5. Comparison of textural characterization and microstructure of the solids obtained in this study with those found in the literature (continuation).

	Synthetic route[a]					***Data found in the literature***					
Sample	***Iron source[b]; Additive[c]***	***Method***	***pH***	***T of ageing (ºC)***	***Time (h)***	***BET surface area (m^2/g)***	***Average pore size (nm)***	***Pore Volume (cm^3/g)***	***Particle Size: TEM (nm)***	***Morphology***	***Reference***
Goethite	Fe(III) salt; No additive	Sol-gel[d]	11-12	25-120	48-288	n.a.	n.a.	n.a.	Length: 202 to 282; Width: 16 to 86	Rod or Lath-like particles	[28]Thies-Weesie et al., 2007
Goethite	Fe(III) salt; With additives	Micro-emulsion and precipi-tation[e]	n.a.	90	2-6	n.a.	n.a.	n.a.	Length: 60 to 150; Width: 7	Nanotubes	[29]Yu et al., 2007

[a]Implying batch system. [b]Fe(III) salt: $Fe(NO_3)_3 \cdot 9H_2O$ or $FeCl_3$ [c]Additives: hydrazine sulphate, oleic acid, and xylene. [d]Alkaline source: NaOH or NH_4OH [e]Precipitating agent: CH_3CH_2OH.
n.a.: Not reported.

Table S5. Comparison of textural characterization and microstructure of the solids obtained in this study with those found in the literature (continuation).

	Synthetic route[a]					***Data found in the literature***					
Sample	***Iron source[b]; Additive[c]***	***Method***	***pH***	***T of ageing (ºC)***	***Time (h)***	***BET surface area (m^2/g)***	***Average pore size (nm)***	***Pore Volume (cm^3/g)***	***Particle Size: TEM (nm)***	***Morphology***	***Reference***
Goethite	Fe(III) salt; With additive	Sol-gel[d]	12	90	72	n.a.	n.a.	n.a.	Length:90-152; Width:10-14	Nanorods	[30]Lee Penn et al., 2006
Goethite	Fe(III) salt; No additive	Precipi-tation[e]	1.7-8	25	> 0.25	280-316	1.7-8.8	0.22-0.47	Largest dimension: 2-10	Spongy mass. Not well defined nanorods	[31]Bakoyannakis et al., 2003

[a]Dialysis (semicontinuous reactor). [b]Fe(III) salt: $Fe(NO_3)_3 \cdot 9H_2O$, $FeCl_3 \cdot 6H_2O$ or $Fe_2(SO_4)_3 \cdot xH_2O$. [c]Additive: $NaHCO_3$. [d]Alkaline source (OH): NaOH. [e]Precipitating agent: $(NH_4)_2CO_3$ or $NH_2CO_2NH_4$.
n.a. Not reported.

Table S5. Comparison of textural characterization and microstructure of the solids obtained in this study with those found in the literature (continuation).

	Synthetic route[a]					***Data found in the literature***					
Sample	***Iron source[b]; Additive***	***Method[c]***	***pH***	***T of ageing (ºC)***	***Time (h)***	***BET surface area (m^2/g)***	***Average pore size (nm)***	***Pore Volume (cm^3/g)***	***Particle Size: TEM (nm)***	***Morphology***	***Reference***
Goethite	Fe(III) salt; No additive	Sol-gel	n.a.	80	48	40.20-47.05	n.a.	n.a.	n.a.	n.a.	[32]Kosmulski et al., 2003
Goethite	Fe(III) salt; No additive	Sol-gel	G1: 3-13	G1: 95	G1:168	G1: 51.3	G1: 28.36-32.20	G1:0.404	G1: Length: 400 ± 50; Width :15 ± 5	G1: Highly acicular	This study
			G2: 3-13	G2: 95	G2:168	G2: 53.6	G2: 22.07-23.95	G2:0.322	G2: Length: 950 ± 100; Width :140 ± 20	G2: Moderately acicular	

[a]Implying batch system. [b]Fe(III) salt: $Fe(NO_3)_3$ or $FeCl_3 \cdot 6H_2O$ [c]Precipitating agent: KOH or NaOH
n.a.: Not reported.

Table S5. Comparison of textural characterization and microstructure of the solids obtained in this study with those found in the literature (continuation).

	Synthetic route[a]					***Data found in the literature***					
Sample	***Iron source[b]; Additive***	***Method[c]***	***pH***	***T of ageing (ºC)***	***Time (h)***	***BET surface area (m^2/g)***	***Average pore size (nm)***	***Pore Volume (cm^3/g)***	***Particle Size: FESEM [e]or TEM [f] (nm)***	***Morphology***	***Reference***
Mixture Goethite-Hematite	Fe(III) salt; No additive	Sol-gel	2.5-13.5	70	24	31.20	n.a.	n.a.	Length[e]: 750±100; Width[e]: 60±20	Highly acicular goethite; no data for hematite	[10]Montes-Hernández et al., 2011
Mixture Goethite-Hematite	Fe(III) salt; No additive	Sol-gel	3-13	95	168	13.2	27.74-31.56	0.102	Length[f]: 880±100; Width[f]: 145±50	Acicular (goethite); Pseudocubic (hematite)	This study (GH)

[a]Implying batch system. [b]Fe(III) salt: $Fe(NO_3)_3 \cdot 9H_2O$ or $FeCl_3 \cdot 6H_2O$. [c]Alkaline source: NaOH or $Ca(OH)_2$.
n.a.: Not reported.

7. References

1. M. Tadic, N. Citakovic, M. Panjan, B. Stanojevic, D. Markovic, Đ. Jovanovic and V. Spasojevic, *J. Alloy. Compd.*, 2012, **543**, 118-124.
2. W. Qin, C. Yang, R. Yi and G. Gao, *J. Nanomater.*, 2011, **2011**, 1-5.
3. W. Hamd, S. Cobo, J. Fize, G. Baldinozzi, W. Schwartz, M. Reymermier, A. Pereira, M. Fontecave, V. Artero, C. Laberty-Robert and C. Sanchez, *Phys. Chem. Chem. Phys.*, 2012, **14**, 13224-13232.
4. I. V. Chernyshova, S. Ponnurangam and P. Somasundaran, *Phys. Chem. Chem. Phys.*, 2010, **12**, 14045-14056.
5. F. M. Michel, L. Ehm, S. M. Antao, P. L. Lee, P. J. Chupas, G. Liu, D. R. Strongin, M. A. A. Schoonen, B. L. Phillips and J. B. Parise, *Science*, 2007, **316**, 1726-1729.
6. H. Tüysüz, E. L. Salabaş, C. Weidenthaler and F. Schüth, *J. Am. Chem. Soc.*, 2007, **130**, 280-287.
7. M. Fleischer, G. Y. Chao and A. Kato, *Am. Mineral.*, 1975, **60**, 485-489.
8. M. Ristić, I. Opačak, J. Štajdohar and S. Musić, *J. Mol. Struct.*, 2015, **1090**, 129-137.
9. C. Wei, P. Qiao, Z. Nan, *Mater. Sci. Eng*: C, 2012, **32**, 1524-1530.
10. G. Montes-Hernandez, P. Beck, F. Renard, E. Quirico, B. Lanson, R. Chiriac and N. Findling, *Cryst. Growth Des.*, 2011, **11**, 2264-2272.
11. M. Ristić, E. De Grave, S. Musić, S. Popović and Z. Orehovec, *J. Mol. Struct.*, 2007, **834–836**, 454-460.
12. E. Murad, *Phys. Chem. Miner.*, 1996, **23**, 248-262.
13. N. Pariona, K. I. Camacho-Aguilar, R. Ramos-González, A. I. Martinez, M. Herrera-Trejo and E. Baggio-Saitovitch, *J. Magn. Magn. Mater.*, 2016, **406**, 221-227.

14. M. Mashlan, R. Zboril, L. Machala, M. Vujtek, J. Walla and K. Nomura, *J. Metastab. Nanocryst.*, 2004, **20-21**, 641-647.
15. R. Zboril, M. Mashlan and D. Petridis, *Chem. Mater.*, 2002, **14**, 969-982.
16. S. Krehula and S. Musić, *J. Cryst. Growth*, 2008, **310**, 513-520.
17. C. Su and D. L. Suarez, *Clay. Clay. Miner.*, 1997, **45**, 814-825.
18. A. M. Jubb and H. C. Allen, *ACS Appl. Mater. Inter.*, 2010, **2**, 2804-2812.
19. M. Gotić and S. Musić, *J. Mol. Struct.*, 2007, **834–836**, 445-453.
20. H. D. Ruan, R. L. Frost and J. T. Kloprogge, *Spectrochim. Acta A*, 2001, **57**, 2575-2586.
21. B. Paul, B. Bhuyan, D. D. Purkayastha and S. S. Dhar, *Catal. Commun.*, 2015, **69**, 48-54.
22. S. Sivakumar, D. Anusuya, C. P. Khatiwada, J. Sivasubramanian, A. Venkatesan and P. Soundhirarajan, *Spectrochim. Acta Part A*, 2014, **128**, 69-75.
23. K. Supattarasakda, K. Petcharoen, T. Permpool, A. Sirivat and W. Lerdwijitjarud, *Powder Technol.*, 2013, **249**, 353-359.
24. H. Liu, Y. Wei, P. Li, Y. Zhang and Y. Sun, *Mater. Chem. Phys.*, 2007, **102**, 1-6.
25. Z. Xu, J. Yu and W. Xiao, *Chem – Eur. J.*, 2013, **19**, 9592-9598.
26. Z. Yan, Z. Xu, J. Yu and M. Jaroniec, *Environ. Sci. Technol.*, 2015, **49**, 6637-6644.
27. M. Mohapatra, K. Rout, S. K. Gupta, P. Singh, S. Anand and B. K. Mishra, *J. Nanopart. Res.*, 2009, **12**, 681-686.
28. D. M. E. Thies-Weesie, J. P. de Hoog, M. H. Hernandez Mendiola, A. V. Petukhov and G. J. Vroege, *Chem. Mater.*, 2007, **19**, 5538-5546.
29. T. Yu, J. Park, J. Moon, K. An, Y. Piao and T. Hyeon, *J. Am. Chem. Soc.*, 2007, **129**, 14558-14559.
30. R. Lee Penn, J. J. Erbs and D. M. Gulliver, *J. Cryst. Growth*, 2006, **293**, 1-4.

31. D. N. Bakoyannakis, E. A. Deliyanni, A. I. Zouboulis, K. A. Matis, L. Nalbandian and T. Kehagias, *Micropor. and Mesopor. Mat.*, 2003, **59**, 35-42.

32. M. Kosmulski, E. Maczka, E. Jartych and J. B. Rosenholm, *Adv. Colloid Interfac.*, 2003, **103**, 57-76.